npj | quantum materials

Review

Published in partnership with Nanjing University

https://doi.org/10.1038/s41535-025-00801-3

Quantum geometry in quantum materials

Jiabin Yu[1,2] ✉, B. Andrei Bernevig[2,3,4], Raquel Queiroz[5], Enrico Rossi[6], Päivi Törmä[7] & Bohm-Jung Yang[8,9,10]

Quantum geometry, characterized by the quantum geometric tensor, plays a central role in diverse physical phenomena in quantum materials. This pedagogical review introduces the concept and highlights its implications across multiple domains, including optical responses, Landau levels, fractional Chern insulators, superfluid weight, spin stiffness, exciton condensates, and electron-phonon coupling. By integrating these topics, we emphasize the broad significance of quantum geometry in understanding emergent behaviors in quantum systems and conclude with an outlook on open questions and future directions.

Quantum materials can be loosely defined as materials for which quantum mechanical effects manifest on a macroscopic scale. Two classes of quantum materials are paradigmatic: superconductors, and quantum Hall systems. For superconductors, electron-electron interaction is the key ingredient that leads to a macroscopic manifestation of quantum mechanics: such interaction causes the electrons to form phase-coherent Cooper pairs and this results in the Meissner effect and the dissipationless transport of charge current. For a two-dimensional (2D) electron gas in the integer quantum Hall regime, the perfect quantization of the Hall conductivity can be understood without explicitly taking any effects of electron-electron interactions into account. The integer quantum Hall effect (QHE) can be attributed to the unique topology of the free-electrons' ground state[1]. Such topology is encoded by the Chern number, C, given by the integral over the Brillouin zone of the Berry curvature that measures the change of the eigenstate's phase as the momentum $\boldsymbol{k}$ is varied. The Berry curvature is part of the *quantum geometry* of a material. The QHE is the archetypical demonstration that quantum geometry is one of the key quantities that make a material a *quantum material*. As we will discuss in the remainder of the review, the Berry curvature turns out to be the antisymmetric part of a tensor Q, the quantum geometric tensor (QGT)[2]. In recent years it has become apparent that the symmetric part of this tensor, the quantum metric, g, also plays a key role in making a material, quantum. In a loose sense, the quantum metric appears to be the key quantity to understand the properties of materials in which both interactions and quantum geometry lead to macroscopic manifestations of quantum mechanics.

Quantum geometry is the geometric structure that naturally arises in the space of quantum states when such states depend on continuous parameters. One classic example of quantum geometry is the geometric phase of a quantum state under adiabatic evolution, in which case the continuous parameter is time. Within condensed matter physics, the continuous parameters are the components of the crystal momentum $\boldsymbol{k}$, and quantum geometry refers to the geometric properties of the Bloch states, more precisely, the periodic part of the Bloch states $|u_{\boldsymbol{k}}\rangle$, which is the focus of this review. In this context, quantum geometry is also called band geometry, which includes long-known concepts such as the spread of the possible Wannier basis and the parallel transport of the electronic states.

The QGT (also called the Fubini-Study metric[3,4]) has components:

$$Q_{ij}(\boldsymbol{k}) = \langle \partial_{k_i} u_{\boldsymbol{k}} | [\mathbb{1} - |u_{\boldsymbol{k}}\rangle\langle u_{\boldsymbol{k}}|] | \partial_{k_j} u_{\boldsymbol{k}} \rangle, \tag{1}$$

where k_i is the ith component of the Bloch momentum $\boldsymbol{k}$. For simplicity in writing Eq. (1) we have considered the case of a well-isolated band. The antisymmetric part of $Q_{ij}(\boldsymbol{k})$ is $\mathrm{i}B_{ij}(\boldsymbol{k}) = [Q_{ij}(\boldsymbol{k}) - Q_{ji}(\boldsymbol{k})]/2$ is related to the well known Berry curvature[5–7] $F_{ij}(\boldsymbol{k})$ as $B_{ij}(\boldsymbol{k}) = -F_{ij}(\boldsymbol{k})/2$, and the symmetric part $g_{ij}(\boldsymbol{k}) = [Q_{ij}(\boldsymbol{k}) + Q_{ji}(\boldsymbol{k})]/2$ is the quantum metric g given that corresponds to the metric for infinitesimal distances of the Hilbert-Schmidt quantum distance $d_{\mathrm{HS}}(\boldsymbol{k}, \boldsymbol{k}') \equiv \sqrt{1 - |\langle u_{\boldsymbol{k}} | u_{\boldsymbol{k}'}\rangle|^2}$: $ds^2 = \sum_{i,j} g_{ij}(\boldsymbol{k}) dk_i dk_j$.

In two dimensions (2D) the integral over the Brillouin Zone (BZ) of $B_{xy}(\boldsymbol{k})/\pi$ for the states of an occupied band is quantized and equal to the Chern number C. Conversely, the integral of $g_{ij}(\boldsymbol{k})$ over the BZ is in general not quantized. However, in 2D, the positive semidefinite nature of Q (combined with inequality between trace and determinant) implies the following inequalities[8]

$$\mathrm{Tr} g(\boldsymbol{k}) \geq 2\sqrt{\det g(\boldsymbol{k})} \geq 2|B_{xy}(\boldsymbol{k})| \tag{2}$$

We can introduce the tensor $M \equiv (1/\pi)\int_{BZ} d^d\boldsymbol{k} Q(\boldsymbol{k})$. Because M is a sum of positive semidefinite tensors, it is itself positive semidefinite, and so $\det M \geq 0$. In 2D this leads to the inequality $\det(\mathrm{Re}(M)) \geq \det(\mathrm{Im}(M))$, that can be seen as the integral equivalent of Eq. (2), and can be written as

$$\det\left[\frac{1}{\pi}\int d^2k\, g(\boldsymbol{k})\right] \geq \det\left[\frac{1}{\pi}\int d^2k\, B(\boldsymbol{k})\right] = C^2. \tag{3}$$

[1]Department of Physics, University of Florida, Gainesville, FL, USA. [2]Department of Physics, Princeton University, Princeton, NJ, USA. [3]Donostia International Physics Center, Sebastian, Spain. [4]IKERBASQUE, Basque Foundation for Science, Bilbao, Spain. [5]Department of Physics, Columbia University, New York, NY, USA. [6]Department of Physics, William & Mary, Williamsburg, VA, USA. [7]Department of Applied Physics, Aalto University School of Science, Aalto, Finland. [8]Department of Physics and Astronomy, Seoul National University, Seoul, South Korea. [9]Center for Theoretical Physics (CTP), Seoul National University, Seoul, South Korea. [10]Institute of Applied Physics, Seoul National University, Seoul, South Korea. ✉e-mail: yujiabin@ufl.edu

Eq. (3) is a classic example of topology bounding quantum geometry from below[9]. The generalization of Eq. (3) leads to the lower bound of quantum geometry due to the Euler number[10–13] (the generalization is most natural in the Chern gauge for the Euler bands), and the lower bound has also been derived for obstructed atomic limits[14] and chiral winding number[15]. Recently, the lower bound of quantum geometry has also been derived[16] for the time-reversal protected Z_2 topology[17–20]. These topological bounds allow us to put a lower bound to the geometric contribution to quantities such as the superfluid weight, as discussed in section “Superconductivity and superfluidity”.

The quantization in 2D of the integral of $B_{ij}(\boldsymbol{k})/(2\pi)$ over the BZ, and its direct relation to the off-diagonal conductivity σ_{xy}[1] made the study of the physical consequences of the anti-symmetric part of $Q(\boldsymbol{k})$ one of the most active areas of research in condensed matter physics for the past 20 years. It has led to several discoveries, such as topological insulators (TIs) and superconductors[21–23], Weyl and Dirac semimetals (SMs)[24–26], and, more recently, higher order topological materials[27–32]. Conversely, the study of the symmetric part of $Q(\boldsymbol{k})$ has received much less attention largely due to the fact until recently $g(\boldsymbol{k})$ had only been shown to contribute to quantities that are challenging to measure experimentally, like the Hall viscosity[33–41], and the ‘Drude weight”, D, of the electrical conductivity of *clean systems at zero temperature*[42–46]. Theoretical and experimental developments in the last few years have profoundly changed the situation. First, it was shown that g is related to nonlinear responses[47–57]. It was further pointed out that g contributes to the superfluid weight (same as superfluid stiffness) $\left[D_s\right]_{ij}$ of a superconductor[10,58–66], and that such contribution is significant when the bandwidth of the bands crossing the Fermi energy is smaller than the superconducting gap. Both nonlinear responses and $\left[D_s\right]_{ij}$ could in principle be measured in realistic experimental conditions. In addition, the realization of magic-angle twisted bilayer graphene (TBG)[67–80] and other twisted materials[81–83] introduced experimentally accessible systems with extremely flat bands exhibiting superconductivity and Fractional Chern Insulator/Ferromagnetism for which the quantum metric contribution to the superconducting $\left[D_s\right]_{ij}$ or to the magnon stiffness can be large. These developments have motivated a huge interest in understanding the role of g_{ij} in quantum materials.

We now discuss more in detail how the quantum metric affects the properties of condensed matter systems. However, it is worth emphasizing that, besides condensed matter physics, the quantum metric plays a role in many other areas of physics, such as metrology, via the closely related concept of quantum Fisher information[84], non-equilibrium dynamics[50], and quantum information science[85,86].

Simple two-bands model

To gain some intuition about quantum geometry, it is useful to consider a simple two-band model described by the following Hamiltonian $h(\theta,\varphi) = \boldsymbol{d}(\theta,\varphi)\cdot\boldsymbol{\sigma}$ where $\boldsymbol{\sigma} = (\sigma_x, \sigma_y, \sigma_z)$ is the vector formed by the 2×2 Pauli matrices and

$$\boldsymbol{d} = (\sin(J_\theta\theta)\cos(J_\varphi\varphi), \sin(J_\theta\theta)\sin(J_\varphi\varphi), \cos(J_\theta\theta)). \tag{4}$$

with J_θ, J_φ, two integers. The energy eigenvalues are $\epsilon_\pm = \pm|\boldsymbol{d}(\theta,\varphi)| = \pm 1$. The eigenvalues $\epsilon_\pm$ do not depend on the variables θ and φ that parametrize h and therefore describe two flat bands. The variables θ and φ only affect the energy eigenstates: $\nu_- = (\sin(J_\theta\theta/2)e^{-iJ_\varphi\varphi}, -\cos(J_\theta\theta/2))^T$, $\nu_+ = (\cos(J_\theta\theta/2)e^{-iJ_\varphi\varphi}, \sin(J_\theta\theta/2))^T$.

In the limit $J_\theta = J_\phi = 0$ also the eigenstates do not depend on θ and φ a and therefore the QGT is identically zero; the Hamiltonian describes a system with no quantum geometry. If we associate the degree of freedom described by the Pauli matrices to a sublattice degree of freedom, this case can be visualized as the situation in which in each energy eigenstate the electrons are completely localized on one of the two “sublattices” (entries of the spinor wavefunction), as shown schematically in Fig. 1a, c.

When $J_\theta = J_\phi = 1$ the eigenstates depend on θ and φ and therefore the two bands possess a non-trivial quantum geometry. Using the expression above for ν_-, and the definition Eq. (1) of the QGT (with k_i $(i = 1, 2)$ running over the labels (φ, θ)) for the lowest band we find

$$Q_{ij}(\varphi,\theta) = \begin{pmatrix} \frac{\sin^2\theta}{4} & \mathrm{i}\frac{\sin\theta}{4} \\ -\mathrm{i}\frac{\sin\theta}{4} & \frac{1}{4} \end{pmatrix} \tag{5}$$

As expected the anti-symmetric part of the QGT is equal to −1/2 the Berry curvature[87]. It is straightforward to verify that the inequalities in Eq. (2) are satisfied. Figure 1b, d illustrate the dependence of the eigenstates on the variables that parametrize the Hamiltonian: the dependence on θ and φ of the hybridization of the two degrees of freedom is responsible for a nonzero QGT. In the case of a sublattice, this can be visualized as a dependence on θ of the relative weight of the electron wave function between the sublattices, Fig. 1d.

For the case in which H describes electrons with a two-fold degree of freedom (sublattice, spin, or a generic orbital degree of freedom) a nonzero anti-symmetric part of Q_{ij} can result in a contribution to off-diagonal (transverse) transport coefficients. For instance, for $J_\theta = J_\phi = 1$ our simple model exhibits a Chern number $C = 1$[87] that can be associated with a nonzero and quantized Hall conductivity, and therefore the presence of delocalized electronic states. Similarly, the real part of $Q_{ij}(\boldsymbol{k})$ can result in a contribution to *diagonal* (longitudinal) transport coefficients. For instance, in this example, in the metallic regime, when the band is not completely filled, one would expect the Drude weight D to be zero given that the band is

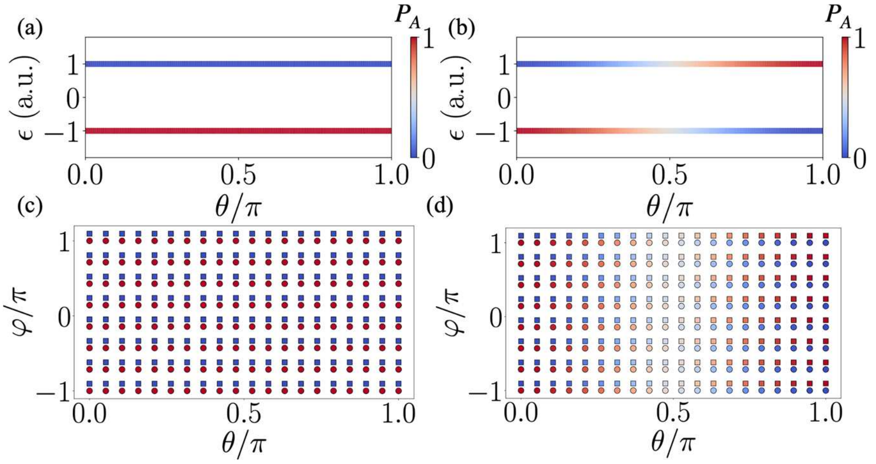

Fig. 1 | Schematic spectra and states hybridization for a simple two-level model in which the two-fold degree of freedom is mapped to a sublattice, {*A*, *B*}. a, b Energy eigenvalues as a function of θ for the case when $J_\theta = J_\phi = 0$ and $J_\theta = J_\phi = 1$, respectively. The colors show the occupation probability of sublattice A, P_A. **c, d** Representation of the lowest energy eigenstate distribution, as function of θ and φ, between sublattice A, represented by circles, and sublattice B, represented by squares, and the color showing the probability occupation of each sublattice, for $J_\theta = J_\phi = 0$ and $J_\theta = J_\phi = 1$, respectively. For the probabilities, P_A, P_B, on each sublattice we use the same color scheme used for P_A in (**a**, **b**).

completely flat and $D \sim n/m^*$, with n the electron's density and m^* the electron's effective mass, i.e., the curvature of the bands. However, the fact that $g_{ij}(\boldsymbol{k})$ is nonzero results in a nonzero Drude weight[43,44], current noise[88], and a quantum geometric dipole[89], signaling that even if the band is completely flat, the system can respond, in the ideal case, to an external d.c. electric field. This is an indication that some states in this band are not completely on-site localized.

It is interesting to consider the limit $J_\varphi = 0$, $J_\theta = 1$. In this case, h is parametrized by only one variable, θ, and therefore the Berry curvature, and so the anti-symmetric part of $Q_{ij}(\boldsymbol{k})$, are identically zero. Nevertheless, the quantum metric is still not zero: $g_{\theta\theta} = 1/4$. This simple example is an extreme case of the important fact that the quantum metric can be nonzero even if the Berry curvature is zero. As Eq. (2) shows, the quantum metric is only bounded from below by the Berry curvature.

Localization tensor

The QGT tensor is not limited to the single-band case—it can be defined for an isolated set of any number of bands. Of common interest is the set of occupied bands of a band insulator, for which the QGT reads

$$\left[Q_{ij}(\boldsymbol{k})\right]_{mn} = \left\langle \partial_{k_i} u_{m\boldsymbol{k}} | [\mathbb{1} - P_{\boldsymbol{k}}] | \partial_{k_j} u_{n\boldsymbol{k}} \right\rangle, \tag{6}$$

where $P_{\boldsymbol{k}} = \sum_{n \in \text{occ.}} |u_{n\boldsymbol{k}}\rangle\langle u_{n\boldsymbol{k}}|$. (Throughout the review, we will focus on the case of fully-filled bands unless specified otherwise.) There is a very physical connection between the QGT in Eq. (6) and the localization of the electronic wavefunctions. This connection is imprinted in the linear response of materials when subjected to applied electric or magnetic fields; it follows naturally from the fact that the QGT defined in Eq. (6), when integrated over the Brillouin zone and traced over all occupied bands,

$$\mathcal{Q}_{ij} = \sum_{n \in \text{occ.}} \int_{\text{BZ}} \frac{d^d k}{(2\pi)^d} \left[Q_{ij}(\boldsymbol{k})\right]_{nn}, \tag{7}$$

with d the spatial dimension. $\mathcal{Q}_{ij}$ can be recast as the ground state dipole-dipole correlator

$$\mathcal{Q}_{ij} = \langle r_i (1 - P) r_j \rangle = \frac{1}{\mathcal{V}} \text{Tr}[P r_i (1 - P) r_j P] \tag{8}$$

where $P = \sum_{\boldsymbol{k} \in \text{BZ}} \sum_{n \in \text{occ.}} |\psi_{n\boldsymbol{k}}\rangle\langle\psi_{n\boldsymbol{k}}|$ is the projector in the occupied subspace. Here $\langle \boldsymbol{r} | \psi_{n,\boldsymbol{k}} \rangle = e^{i\boldsymbol{k}\cdot\boldsymbol{r}} \langle \boldsymbol{r} | u_{n,\boldsymbol{k}} \rangle$ is the Bloch state for the nth band, and henceforth, we choose the unit system in which

$$\hbar = 1, \tag{9}$$

unless specified otherwise The position matrix elements are defined for Bloch states[90]

$$\langle u_{n\boldsymbol{k}} | r_i | u_{m\boldsymbol{k}'} \rangle = \delta_{\boldsymbol{k},\boldsymbol{k}'} \left[A_i(\boldsymbol{k})\right]_{mn} + i \delta_{mn} \partial_{k_i} \delta_{\boldsymbol{k},\boldsymbol{k}'}, \tag{10}$$

where $\delta_{\boldsymbol{k},\boldsymbol{k}'} = (2\pi)^d \delta(\boldsymbol{k} - \boldsymbol{k}')/\mathcal{V}$, $\mathcal{V}$ the total volume, and $\left[A_i(\boldsymbol{k})\right]_{nm} = i\langle u_{n\boldsymbol{k}} | \partial_{k_i} | u_{m\boldsymbol{k}} \rangle$. The projector 1—$P$ guarantees that Eq. (8) is gauge independent, by removing the diagonal contributions of the position operator. The integrated geometric tensor $\mathcal{Q}_{ij}$, whose symmetric part and anti-symmetric parts contain the integrated quantum metric and the Chern number of the ground state, can be interpreted as a localization tensor originating in the uncertainty of the position operator in the ground state[42]. First discussed by Kohn[91], a divergent $\mathcal{Q}_{ij}$ would correspond to an infinite sensitivity of the ground state to a shift in momentum or a twist in boundary conditions. Among other definitions based on a spectral gap, this definition based on spatial delocalization of the wavefunction is one of the most suited ways to discriminate between a metal and an insulator. Its geometrical interpretation was then put forward by Resta[92], and Souza, Wilkens, and Martin[93].

The localization tensor has deep consequences in both the constraints on the basis functions that can be used to describe a given band subspace. To understand the spatial extent of electronic bands, it is useful to adopt Wannier states, localized in real space to describe Bloch bands[94]. They are defined as

$$|w_{n\boldsymbol{R}}\rangle = \frac{1}{\sqrt{N}} \sum_{\boldsymbol{k} \in \text{BZ}} e^{-i\boldsymbol{k}\cdot\boldsymbol{R} + \varphi(\boldsymbol{k})} |\psi_{n\boldsymbol{k}}\rangle$$

where N is the number of lattice sites, and $\varphi_n(\boldsymbol{k})$ is a momentum-dependent phase redundancy, which can be tuned to optimize the localization of the Wannier states $|w_{n\boldsymbol{R}}\rangle$. This localization is characterized by the localization functional $\Omega = \sum_n [\langle w_{n\boldsymbol{0}} | r^2 | w_{n\boldsymbol{0}} \rangle - \langle w_{n\boldsymbol{0}} | \boldsymbol{r} | w_{n\boldsymbol{0}} \rangle^2]$[95]. While not gauge independent, Ω can be separated into a gauge independent part that coincides with the trace over spatial indices of the integrated quantum metric, often referred to as $\Omega_I = (\mathcal{V}/N)\text{Re}(\text{Tr}\mathcal{Q})$, and a gauge dependent part $\tilde{\Omega}$ (see Supplementary Information A). The gauge-dependent part $\tilde{\Omega}$ diverges in the absence of exponentially localized Wannier functions. This happens for metals, or in the presence of a nonzero Chern number[96]. An extended review of these results is presented in Supplementary Information A.

Quantum geometry and correlated states

Superconductivity and superfluidity

Superconductivity is fundamentally influenced by the spread of the Wannier states and hence by quantum geometry: the superfluid weight (superfluid stiffness) D_s has a contribution that arises from quantum geometry, $D_{\text{s,geom}}$, in addition to the conventional one $D_{\text{s,conv}}$ given by band dispersion[58]:

$$D_s = D_{\text{s,conv}} + D_{\text{s,geom}}\,. \tag{11}$$

The superfluid weight relates the DC, long-wavelength supercurrent $\boldsymbol{J}$ to the static, long-wavelength, transverse vector potential $\mathcal{A}$:

$$J_i = -\sum_j \left[D_{\text{s}}\right]_{ij} \mathcal{A}_j \tag{12}$$

and needs to be positive-definite for supercurrent to exist. Moreover, in the simplest picture, large $\mathcal{D}_{\text{s}} = \text{Tr}[D_{\text{s}}]/d$ means a large critical current of superconductivity, $j_c \propto \mathcal{D}_{\text{s}}/\xi$, where ξ is the coherence length of the superconductor. In two dimensions, D_{s} also determines the critical temperature of superconductivity since the Berezinskii-Kosterlitz-Thouless (BKT) temperature T_{BKT} depends on $\mathcal{D}_{\text{s}}$. In 3D the penetration depth λ is directly proportional to $1/\sqrt{\mathcal{D}_{\text{s}}}$. A finite value of λ is crucial for the Meissner effect. Given that $\mathcal{D}_{\text{s}}$ is the proportionality constant entering the London equation Eq. (12), the equation responsible for the Meissner effect, and its relation to T_{BKT} in 2D and to λ in 3D, it is a fundamental defining quantity of superconductivity. Interestingly, D_{s} has an intrinsic connection to quantum geometry.

The quantum geometric contribution of superconductivity becomes dramatic in a flat Bloch band. The conventional contribution of superfluid weight $D_{\text{s,conv}}$ is inversely proportional to the effective mass of the band and vanishes in a flat band. Superconductivity in a flat band is thus completely based on quantum geometric effects. Such effects arise since D_s is defined via the current-current correlator[97], and the current operator of a multiband system has two parts (m,n are band indices and $i = x, y, z$):

$$\langle u_{m\boldsymbol{k}} | J_i | u_{n\boldsymbol{k}} \rangle = \delta_{mn} \partial_{k_i} \epsilon_{n\boldsymbol{k}} + (\epsilon_{m\boldsymbol{k}} - \epsilon_{n\boldsymbol{k}}) \left\langle \partial_{k_i} u_{m\boldsymbol{k}} | u_{n\boldsymbol{k}} \right\rangle, \tag{13}$$

Here $\boldsymbol{k}$ is the momentum and $\epsilon_{n\boldsymbol{k}}$ gives the dispersion for the nth band. The last term, which contains a derivative of the Bloch function, connects D_{s} to the quantum geometric quantities defined in the introduction.

Full formulas of $D_{\mathrm{s}} = D_{\mathrm{s,conv}} + D_{\mathrm{s,geom}}$ are available in the literature[58,60,98]. The result is the following in the limit of N_{f} completely flat degenerate bands, isolated from other bands by large gaps compared to the attractive interaction energy scale $|U|$, assuming zero temperature and time-reversal symmetry, and under so-called uniform pairing condition where pairing is the same in all the flat band orbitals:

$$[D_s]_{ij} = \frac{4e^2 N_{\mathrm{f}}}{(2\pi)^{d-1} N_{\mathrm{orb}}} |U| f(1-f) \mathcal{M}_{ij}^{\mathrm{min}}, \tag{14}$$

$$\mathcal{M}_{ij}^{\mathrm{min}} = \frac{1}{2\pi}\left[\int \mathrm{d}^d \boldsymbol{k}\, g_{ij}(\boldsymbol{k})\right]_{\mathrm{min}}. \tag{15}$$

Here, $f \in [0, 1]$ is the filling fraction of the isolated flat band, N_{orb} is the number of orbitals where the flat band states have a nonzero amplitude, $-e$ is the electron charge, d is the space dimension, and $g_{ij}(\boldsymbol{k})$ is the quantum metric defined in the introduction. The label "min" refers to the integrated quantum metric whose trace is minimal under variation of the orbital positions while keeping all other parameters, e.g., hoppings, the same. (Equivalently, it is minimal under the change of Fourier transformation convention of the atomic basis, which is equivalent to the embedding choice.) This result is in striking contrast with the simple Bardeen-Cooper-Schrieffer (BCS) formula for a single band, $\mathcal{D}_{\mathrm{s}} = e^2 n_{\mathrm{s}}/m^*$, where n_{s} is the density of Cooper pairs (superfluid density) and m^* the effective mass. The result (14)–(15) was essentially derived in ref. 58, but in ref. 98 it was noted that the $\mathcal{M}_{ij}$ of the original work[58] has to be replaced by $\mathcal{M}_{ij}^{\mathrm{min}}$ because the quantum metric is an embedding (or, basis) dependent quantity[99] while D_{s} and $\mathcal{M}_{ij}^{\mathrm{min}}$ are embedding-independent[98,100]. These results are derived within multiband mean-field theory, but the general idea has been confirmed by exact, perturbative and beyond-mean-field numerical calculations[15,59,60,101–104] of some carefully chosen attractive interacting flat band models (see the reviews[63,64,105] for more examples). We note that in most of the beyond-mean-field numerical calculations, what one directly calculates is the stiffness of a SU(2) pseudo-spin ferromagnet, which after adding additional terms becomes a superconductor. In refs. 106,107, it has been shown that many of the analytical results presented in[58,98] can be extended to several cases of non-uniform pairing and the results remain essentially similar. The effect of closing the gap between the flat band and other bands has been studied as well, see ref. 108 and references therein.

How should one physically understand the role of the quantum metric in flat-band superconductivity? One way to gain intuition is to consider the two-body problem, the Cooper problem[109], in a flat band. In this case there is a massive degeneracy which, however, is lifted by the interaction between the two particles: the bound pair becomes dispersive, with an inverse effective mass given by the quantum metric[110]! Similar to the Fermi surface Cooper problem, the two-body problem in the flat band gives essentially the same answer as the mean-field approach. Further insight into why quantum geometry may be critical for pair mobility is provided by its connection to the localization of Wannier functions, as discussed in the introduction[94]. Indeed, by projecting the interacting multiband model to a flat band[15] one can show that interactions induce pair hopping that is linearly proportional to the interaction U—and overlap integrals of Wannier functions at neighboring sites. In 2D this relates nicely to the lower bound of superconductivity derived in ref. 58: $\mathcal{D}_{\mathrm{s}} \geq |C|$ (in appropriate units), where C is the spin Chern number of a time-reversal symmetric system; as Wannier functions cannot be exponentially localized in a topological band[96], their overlaps guarantee interaction-induced motion and eventually superconductivity. The role of Wannier functions in superconductivity offers routes for deriving upper bounds too. For example, the optical spectral weight of a superconductor and superfluid weight were considered in refs. 111,112, where quantum geometric quantities appeared as key quantities. For further information and discussion of the large literature on this topic, we refer to existing review articles[63,64,105]. Here we would like to mention only a few interesting developments published after these review articles.

In refs. 113–115, a Ginsburg-Landau theory was developed for multiband systems, with quantum geometry in focus. According to these works, in the isolated flat band limit and with uniform pairing, the coherence length of the superconductor is determined by the minimal quantum metric. For non-isolated flat bands, the coherence length can be smaller than the quantum geometry length[116]. Furthermore, for strong interactions the Cooper pair size and the coherence length may be distinct, resembling the BEC-end of the BEC-BCS crossover[117]. In ref. 118 a definition of the coherence length based on the exponential decay length of the anomalous Green's function was used, leading to a result that differs from the minimal quantum metric. The decay of the pair correlation function or the anomalous Green's function can be non-trivial in flat bands. For example, they may completely vanish beyond a few lattice sites, instead of exhibiting a continuous decay[118,119]. This happens in flat bands that host compactly localized Wannier functions (such as obstructed atomic limits[120]).

The apparent discrepancy between the coherence length results can be explained through the subtlety of the definition of this concept in flat bands. The mean-field anomalous Green's function and the pair correlation function may decay rapidly in length scales different from the minimal quantum metric, however, when one includes *fluctuations* of the order parameter and calculates the spread of the pair correlation function, a coherence length given by the minimal quantum metric is obtained. Fluctuations are included in the Ginzburg-Landau formalism like in the calculation of the superfluid weight (stiffness), so, naturally, dependence on quantum geometry emerges from both. Reference[119] studied a superconductor-normal-superconductor (SNS) Josephson junction where the normal part is a flat band system longer than the coherence length. It was found that supercurrent over the junction was only possible by contributions from nearby dispersive bands or by interaction-mediated transport.

One might worry that disorder would kill flat band superconductivity. However, D_s for a flat band, s-wave, superconductor with non-trivial quantum metric appears as robust against non-magnetic disorder as D_s for a superconductor with dispersive bands and trivial quantum metric[121]. Interestingly, the dispersive band superfluid weight acquires a geometric contribution in the presence of disorder that at low disorder strengths compensates the suppression of the conventional contribution; this is intuitive as disorder hinders conventional ballistic transport given by the band dispersion. Quantum geometry has been shown to be relevant for correlations in disordered systems also in other contexts than superconductivity[122,123]. Another salient feature of flat band superconductors is that quasiparticles seem to be localized[124]. Finally, it is important to keep in mind that although the quantum geometry of the band guarantees superconductivity to be possible, sometimes another competing order, e.g., a charge density wave or phase separation, can win[125] even with attractive interactions. Quantum geometry can also lead to pair-density wave order instead of superconductivity, signified by a negative superfluid weight[126,127]. Quantum geometry may also affect the Kohn-Luttinger mechanism of superconductivity because the form factor in the polarization function responsible for screening depends on the geometric properties of the wave functions[128,129]; remarkable enhancements of the critical temperature were found in these works for certain model systems.

Spin-wave stiffness

The close analogy between superconductivity and the XY model[130,131] suggests the connections shown in the previous section between quantum geometry and the properties of superconductors should be relevant for ferromagnetic states in which the ground state is characterized by an order parameter $\boldsymbol{M}$ that breaks a continuous spin, or pseudospin, symmetry. In the continuum limit, this can be seen by considering the effective Ginzburg-Landau action of a ferromagnet

$$S = S_0(\boldsymbol{M}) + \beta\frac{1}{2}\int d\boldsymbol{r}\,\mathcal{D}_s^{(s)}[|\nabla M_x|^2 + |\nabla M_y|^2 + |\nabla M_z|^2] \tag{16}$$

where $\boldsymbol{M}$ is the magnetization and S_0 is the part of the action that does not depend on the gradient of $\boldsymbol{M}$. In Eq. (16), we have assumed the spin stiffness tensor to be diagonal and isotropic: $[D_s^{(s)}]_{ij} = \mathcal{D}_s^{(s)}\delta_{ij}$.

Similar to superconductivity, the spin-stiffness $[D_s^{(s)}]_{ij}$ can be obtained within linear response theory by calculating the spin susceptibility, $\chi_{ij}^{(s)}(\boldsymbol{q}, \omega)$, and then taking the limit $\omega = 0$, $\boldsymbol{q} \to 0$: $[D_s^{(s)}]_{ij} = \lim_{\boldsymbol{q}\to 0}\chi_{ij}^{(s)}(\boldsymbol{q}, \omega = 0)$. Starting from a microscopic model, it is straightforward to see that the expression of $\chi^{(s)}(\boldsymbol{q}, \omega = 0)$ up to order $\boldsymbol{q}^2$, involves the first and second derivatives of the Hamiltonian with respect to the momentum $\boldsymbol{k}$. For single-band systems, such derivatives lead only to the appearance of derivatives with respect to $\boldsymbol{k}$ of the energy eigenvalues, similarly to the first term of Eq. (13). However, for multi-band systems, the second term in Eq. (13) appears, involving the quantum geometry of the Bloch states.

In superconductors, the superfluid stiffness is directly proportional to the superfluid weight and so it can be directly probed by measuring the current response to an external vector field. For ferromagnetic states, the most straightforward way to probe QGT's effects is by probing the dispersion of the low-energy spin-waves, i.e., the Goldstone modes associated to the continuous symmetry spontaneously broken by the ground state, something that is not straightforward to do for superconductors[132] also due to the Anderson-Higgs mechanism. For 2D XY ferromagnets, the effect of the quantum geometry can potentially also be inferred indirectly by measuring T_{BKT}, as discussed in the case of superconductors.

So far the role of quantum geometry in ferromagnetic systems—and especially in realistic experimental systems has not received much attention. Recent works have investigated the connection between $[D_s^{(s)}]_{ij}$ for specific systems[133–137]. One can obtain an exact solution of the ferromagnetic ground state and its excitations of a flat band subject to a repulsive interaction in the condition that makes the projected orbital occupation the same[138] (analogous to the uniform pairing condition for superconductors). In this case, the single particle charge excitations are flat. However, the spin wave spectrum can be solved exactly and it can be shown, in this class of models, that the spin stiffness is the same as the integrated minimal quantum metric[138]. In moiré systems, projected Hamiltonians[139,140] do not satisfy the uniform pairing condition, and as such even the single-particle dispersion on top of the ferromagnetic state at integer fillings involves the quantum distance[134]. To exemplify the effect of the quantum metric in ferromagnets in Supplementary Information B we describe the key results for 2D moiré systems[133,134] and saturated ferromagnetism[137].

Bose-Einstein condensation

Superconductivity is closely related to the physics of Bose-Einstein condensation (BEC) of electron pairs, highlighted by the smooth BCS-BEC crossover and a common mean-field ground state for both regimes. Nevertheless, when it comes to the role of quantum geometry, the BEC limit may show quite a different phenomenology from that of superconductors. Quantum geometry describes how the properties of quantum states vary throughout the Brillouin zone. This raises the question: Does quantum geometry have any impact on a (BEC) that occupies a single quantum state? For a non-interacting BEC at equilibrium, quantum geometry is indeed irrelevant. However, when interactions are introduced and excitations are considered, quantum geometry begins to play a significant role. Another natural question is: what is the bosonic counterpart of superconductivity in a flat band? Specifically, where would bosons condense in a flat band where all energies are degenerate? Once again, interactions change the scenario. Due to Hartree-type renormalization of the bands, certain momenta can acquire slightly lower energies, making them favorable sites for condensation[141,142]. This leads to an important question: under what general conditions are such condensates stable? Given that the energies are essentially degenerate, even minimal interactions might excite particles to arbitrary momenta, potentially destabilizing the condensate.

Quantum geometry also plays a crucial role in Bose-Einstein Condensates (BECs). In a weakly interacting BEC within a flat band, the speed of sound-which must be positive to ensure superfluidity-is proportional to the interaction energy U and the square root of a generalized quantum metric[143,144]. Note again the linear dependence on the interaction energy U, typical for flat band phenomena: this is an immediate consequence of the existence of only one energy scale. This should be contrasted to the case of a usual dispersive band where the speed of sound is proportional to $\sqrt{U}$. The stability of a BEC can be also determined by calculating the fraction of excitations, due to weak interactions, that result in a finite particle density outside the condensate state, $n_{\mathrm{ex}}(\boldsymbol{k})$. This is also called the quantum depletion and was found[143] to be given by the condensate *quantum distance* $\tilde{d}_c(\boldsymbol{q})$ (similar to the Hilbert-Schmidt quantum distance d_{HS} defined in the introduction), and, in the limit of vanishing interaction, is related to $n_{\mathrm{ex}}(\boldsymbol{k})$ via the equation

$$\lim_{U\to 0} n_{ex}(\boldsymbol{k}) = \frac{1-\tilde{d}_c(\boldsymbol{q})}{2\tilde{d}_c(\boldsymbol{q})}, \qquad (17)$$

where $\boldsymbol{q} = \boldsymbol{k} - \boldsymbol{k}_{\mathbf{c}}$ and $\tilde{d}_c(\boldsymbol{q})$ includes overlaps of the Bloch state at the condensate momentum $\boldsymbol{k}_{\mathbf{c}}$ with states at other momenta. The physical intuition is that depletion of the condensate to excitations is limited not by energetic reasons as in dispersive bands, but by a finite quantum distance between the initial (ground) and the excited state. The result (17) also implies that quantum excitations on top of the mean-field condensate do not vanish in the limit of small interactions; flat bands are thus an ideal platform for studying the beyond-mean-field physics of condensates. The quantum distance appears instead of the quantum metric because the quantum depletion includes finite momentum excitations. The quantum metric on the other hand is an infinitesimal measure and corresponds to long-wavelength limit quantities such as the speed of sound, and supercurrent in the case of superconductors. Quantum geometry manifests also in the superfluid weight of BEC[144–147].

Exciton condensates

An exciton is a bosonic quasiparticle formed by an electron (e), bound to a hole (h). At low temperatures, a gas of excitons can form an exciton condensate (EC)[148,149]. Due to the effective interaction among excitons, resulting from the Coulomb interaction, an EC will exhibit superfluidity. An EC can be regarded as superfluid BEC, see section "Bose-Einstein condensation". However, it is also analogous to a superconducting state, or a ferromagnetic state, as we discuss in this section.

Shortly after the proposal that electron-hole pairs could form an exciton condensate (EC), it was suggested that spatially separating the electrons and holes would enhance the stability of the EC by reducing the rate of electron-hole recombination[150]. This can be realized in 2D systems formed by an e-doped 2D layer and h-doped 2D layer separated by a high-quality, thin, dielectric film[150,151]. In these double-layer structures, when the doping is sufficiently low, and gates sufficiently far away, so that screening effects are minimized[152,153], an EC can form when the carriers' intralayer distance $\approx \sqrt{1/n}$ is comparable to the interlayer distance d. In such conditions, the layer degree of freedom can be treated as a pseudospin degree of freedom, or as the particle-hole degree of freedom of a superconductor. In the first case the EC can be regarded as an easy-plane ferromagnet (see section "Spin-wave stiffness") in the second case as a "charge neutral superconductor".

We can define the superfluid weight of an EC, in analogy to the definition introduced for a superconductor, as the long-wavelength, zero-frequency, response of the system to a transverse vector field having opposite directions for electrons and holes. For an EC formed in a 2D double-layer this corresponds to having a vector field $\mathcal{A}$ in the top layer and a vector field $-\mathcal{A}$ in the bottom layer. It is then straightforward to derive the expression of $\left[D_s\right]_{ij}$ as done for the superconducting case, (roughly speaking) by reinterpreting the particle-hole index[58,60,98], as the layer index[63,154]. In this analogy, the superconducting order parameter Δ corresponds to the mean-field order parameter describing the EC, $\Delta^{\mathrm{EC}}_{\alpha\alpha',\boldsymbol{r}\boldsymbol{r}'} \equiv \langle c^{\dagger}_{\alpha\boldsymbol{r}T} V_{\mathrm{TB}}(\boldsymbol{r}-\boldsymbol{r}', d) c_{\alpha'\boldsymbol{r}'B}\rangle$, where α (α') is a general orbital degree of freedom, T, B are the indices denoting the

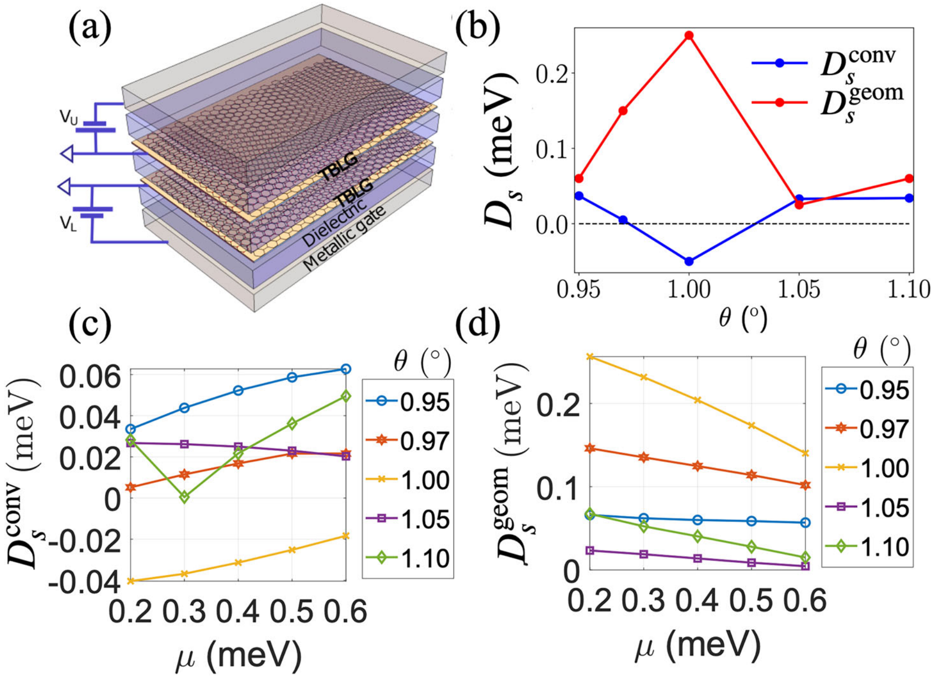

Fig. 2 | Geometric contributions to the superfluid weight. a Schematics of a double layer formed by two TBGs in which an EC state is expected to form when the chemical potential in the top layer μ_T is equal and opposite to the chemical potential in the bottom layer μ_B. **b** Dependence on twist angle of the conventional and geometric contributions to the superfluid weight D_s of an EC formed in a double TBG, for fixed chemical potential $\mu \equiv \mu_T = -\mu_B = 0.2$ mev. **c**, **d** Dependence on μ, for different twist angles, of conventional and geometric contributions, respectively, to D_s. Adapted from ref. 154.

top and bottom layer, respectively, and $V_{\text{TB}}(\boldsymbol{r} - \boldsymbol{r}', d)$ is the effective interlayer Coulomb interaction with d the distance between the layers.

Similar to superconductors, the critical temperature T_c for forming an exciton condensate (EC) is enhanced in flat-band systems. As the bands become flatter, the conventional contribution to the EC's superfluid weight and stiffness is suppressed, reducing the neutral superfluid current and making the EC unstable to thermal and quantum fluctuations despite a high T_c. This changes when flat bands have nontrivial geometry: a geometric contribution to the superfluid weight $\left[D_s\right]_{ij}$ emerges, strengthening the stability of the EC[154,155].

This situation is most apparent in the proposal for an EC formed in a double layer formed by TMDs[155], or by an e-doped TBG and h-doped TBG separated by a thin dielectric layer[154], as schematically shown in Fig. 2a. In this case, for certain twist angles, the conventional contribution to $\left[D_s\right]_{ij}$ can even be negative, as shown in Fig. 2b. However, for the same twist angle, the geometric contribution is positive and very large guaranteeing the stability of the EC, Fig. 2b–d. We see that for an EC the effect of the quantum geometry of the bands can be even more significant than for superconductors.

Electron-phonon coupling

One main interaction in solids is the electron-phonon coupling (EPC), which is crucial for various quantum phases, and in particular for superconductivity[156–158]. It is conceptually intriguing to ask if the EPC has any clear relation to quantum geometry, in particular in the generic case where the electrons have a Fermi surface - characteristic of the great majority of known superconductors. Uncovering this relationship could be crucial for identifying new superconductors, considering the vast array of topological materials[159–166].

Recently, ref. 167 revealed a direct connection between electron band geometry/topology and the bulk electron-phonon coupling (EPC). The study introduces a "Gaussian approximation" where this connection becomes explicit. Within this approximation, a quantum geometric contribution to the electron-phonon coupling constant λ can be naturally distinguished from an energetic contribution. The EPC is the sum of the two (up to a cross-term). (See Supplementary Information C for more details). Explicitly, the geometric contribution is supported by the quantum metric or an extended orbital-selective version of the quantum metric[110,167], and is bounded from below by the topological contributions over the electronic Fermi surface.

The Gaussian approximation can naturally be applied to graphene, where the short-range hopping and the symmetries make it exact, and its generalized version can naturally describe another well-known superconductor, MgB_2. Combined with the ab initio calculation, ref. 167 finds that the quantum geometric (topological) contribution to λ accounts for roughly 50% (50%) and 90% (43%) of the total EPC constant λ in graphene and MgB_2, respectively. The large contributions from quantum geometry to EPC can be intuitively understood: the quantum geometry affects the real-space localization of the electron Wannier functions, and then affects how the electron hopping changes under the motions of ions. This is an important part of the electron-phonon coupling (and in many cases—such as graphene and MgB_2— is the largest part of EPC).

The analysis for graphene in ref. 167 can be tested by measuring the phonon linewidth by Raman spectroscopy as well as measuring phonon frequencies by the inelastic x-ray scattering. Reference 168 found that the quantum metric modifies the electron-phonon coupling by enhancing small-angle scattering. The formalism in ref. 167 can in principle also be applied to other systems such as Weyl semimetals. One major future direction is to develop a general framework that relates quantum geometry to the bulk EPC for realistic systems. Such a study may provide new guidance for the future search for superconductors from the perspective of quantum geometry.

Fractional Chern insulators

Fractional Chern insulators (FCIs) are zero-magnetic-field analogs of the fractional quantum Hall effect. By definition, FCIs should exhibit fractionally quantized Hall resistance and vanishing longitudinal resistance under zero external magnetic field. FCIs were first proposed in toy models[169–171], where fractionally filled nearly flat Chern bands[172,173] (in zero magnetic field) and repulsive interactions are identified as the essential ingredients.

Recall that the fractional quantum Hall effect requires two ingredients: Landau levels (from an external magnetic field) and repulsive interactions. As the repulsive interaction (e.g., Coulomb interaction) is ubiquitous, the special ingredient for the FQH is the Landau level. Therefore, one of the routes (but not the only one) to realizing FCIs is to mimic Landau levels without external magnetic fields.

In this route, quantum geometry plays an important role in assessing how closely a realistic set of bands approximates the Landau levels. Besides its exact flatness and nonzero Chern numbers, the nth Landau level ($n = 0, 1, 2, 3, \ldots$) is characterized by the following three geometric properties: (i) uniform (in momentum space) quantum metric, (ii) uniform (in momentum space) Berry curvature, and (iii) the trace of the quantum metric equals $(2n + 1)$ times the absolute value of the Berry curvature[58,174]. This momentum independence of the LL quantum geometry enabled detailed analytical understanding of the LL physics even in the presence of strong electron-electron interactions[175]. Therefore, the best system for FCIs is the one that hosts nearly flat Chern bands that nearly satisfy those three geometric properties of the Landau levels. References 176–179 suggest that a flat Chern band is already favorable to realize FCIs even as long as an integrated version of (iii) is satisfied, even if (i) and (ii) conditions are strongly violated. (See also refs. 8,180–183). Reference 176,177 promote a concept called "ideal Chern bands", which motivate the study of analogy in other topological bands, such as ideal Euler bands[12]. However, the claims in refs. 176,177 are made for special short-range interactions instead of generic repulsive interactions and for continuum rather than tight-binding models. In practice, as long as a realistic model hosts nearly flat Chern bands near the Fermi level, it is reasonable to consider the possibility of realizing FCIs in such a system, as shown in Supplementary Information D. Besides the way of mimicking Landau levels, one may also carefully desire the interaction to realize FCI in bands with zero Chern number[184].

Moiré systems are natural platforms for FCIs, since the quantum interference owing to moiré superlattice can easily lead to nearly flat topological bands. Upon spontaneous magnetizing due to interactions, these bands become nearly flat Chern bands. Remarkably, last year, FCIs were experimentally realized in twisted bilayer $\mathrm{MoTe_2}$ at fillings $-2/3$ and $-3/5$, as well as integer Chern insulator at filling -1[83,185–191]. Theoretically, the system indeed hosts nearly flat Chern bands that have relatively uniform quantum metric and Berry curvature in each spin subspace[192–211]. Upon spin polarization (Stoner magnetization), the appearance of FCIs follows heuristically from the connection to a single Landau level[198–200,205]. However, as shown in ref. 205, the understanding of the spin properties requires more bands to be considered, i.e., band mixing is essential.

Following the first discovery of FCIs in twisted bilayer $\mathrm{MoTe_2}$, clear evidence of FCIs was later observed in rhombohedral multi-layer graphene-hexagonal boron nitride superlattice (at fractional electron fillings)[212–215], which has almost-fully-connected conduction bands. The theoretical understanding of experimental observations at fractional fillings in those systems requires careful study of various issues, such as the interaction scheme and the roles of temperature and disorder[216–232].

Physical responses

The quantum mechanical uncertainty in the position of electrons in solids, quantified by the QGT $Q_{ij}(\boldsymbol{k})$ in Eq. (1) or its integrated version $\mathcal{Q}_{ij}$ in Eq. (8), leads to physical responses, which will be discussed in this section. For this section, we will resume $\hbar$ explicitly.

Polarization fluctuations

Following fluctuation-dissipation theorems[93,233], the quantum fluctuations of a material's polarization lead to dissipation in the presence of an external field. The electric polarization in solids is obtained[234] by the expectation value of the position operator $p_i = e\langle r_i \rangle$, which can be reduced using Eq. (10) to the integral over the single band Berry connection $\left[A_i(\boldsymbol{k})\right]_{nn}$ in the Brillouin zone. The position fluctuations in the ground state captured by the QGT are therefore associated with polarization fluctuations[235]. They are also hence associated with dissipation in the presence of perturbations that couple with the dipole operator, i.e., in the presence of an applied electric field $\mathcal{E}_i(t) = \mathcal{E}_i e^{i\omega t}$, which modifies the polarization of the medium by the polarizability $p_i(t) = \sum_j \chi_{ij}(t)\mathcal{E}_j(t)$.

To draw the parallel between electric dipole fluctuations of the ground state and quantum geometry, it is convenient to introduce time-dependence to the integrated QGT Eq. (8): $\mathcal{Q}_{ij}(t - t') = \langle r_i(t)(1 - P)r_i(t')\rangle$[236–238]. This captures the fact that virtual interband (dipole) transitions leading to a nontrivial $\mathcal{Q}_{ij}$ are modified in the presence of $\mathcal{E}_i(t)$ by how much time the state populates the virtual bands and how much the position operator has evolved with the static Hamiltonian $\mathcal{H}$. At $t = 0$ it reduces to the integrated QGT (8), but away from the time origin, it has the expression

$$\begin{aligned} \mathcal{Q}_{ij}(t) \;=\; & \mathcal{D}_{ij}(t) + \textstyle\sum_{mn} \int_{\mathrm{BZ}} \frac{d^d k}{(2\pi)^d} f_{n\boldsymbol{k}}\left(1 - f_{m\boldsymbol{k}}\right) \\ & \times \left(\left[\mathfrak{g}_{ij}(\boldsymbol{k})\right]_{nm} + \mathrm{i}\left[\mathfrak{b}_{ij}(\boldsymbol{k})\right]_{nm}\right) e^{i\omega_{mn\boldsymbol{k}} t} \end{aligned} \tag{18}$$

with $\omega_{mn\boldsymbol{k}} = (\epsilon_{m\boldsymbol{k}} - \epsilon_{n\boldsymbol{k}})$, $\epsilon_{n\boldsymbol{k}}$ the dispersion of the nth band, and $f_{n\boldsymbol{k}}$ the occupation factor of the nth band at $\boldsymbol{k}$. Here

$$\begin{aligned} \left[\mathfrak{g}_{ij}(\boldsymbol{k})\right]_{nm} &= \frac{1}{2}\left[A_i(\boldsymbol{k})\right]_{nm}\left[A_j(\boldsymbol{k})\right]_{mn} + (i \leftrightarrow j) \\ \left[\mathfrak{b}_{ij}(\boldsymbol{k})\right]_{nm} &= \frac{1}{2\mathrm{i}}\left[A_i(\boldsymbol{k})\right]_{nm}\left[A_j(\boldsymbol{k})\right]_{mn} - (i \leftrightarrow j)\,, \end{aligned} \tag{19}$$

are the interband metric and curvature matrix elements. It also contains a Fermi surface contribution, $\mathcal{D}_{ij}(t)$, from the second term in the position operator of Eq. (10). The Fermi surface contribution is normally single-band and only present for metals $\mathcal{D}_{ij}(t) = F_{ij} + itD_{ij}$, containing the Drude weight $D_{ij} = \int_{\mathrm{BZ}} \frac{d^d k}{(2\pi)^d} f_{n\boldsymbol{k}} \partial_{k_i}\partial_{k_j}\epsilon_{n\boldsymbol{k}}$ from the dispersion curvature at the Fermi surface; as well as a divergent piece due to the discontinuity at the Fermi surface $F_{ij} = \int_{\mathrm{BZ}} \frac{d^d k}{(2\pi)^d} (f'_{n\boldsymbol{k}})^2 (\partial_{k_i}\epsilon_{n\boldsymbol{k}})(\partial_{k_j}\epsilon_{n\boldsymbol{k}})$. The latter term appears in the real and symmetric part of the geometric tensor, and explains the divergence of the metric for metals, even in single-band metals[239]. The singularities coming from the Fermi surface get regularized by the introduction of a scattering time τ. Finally we note that $\mathcal{Q}_{ij}(t)$ in Eq. (18) has Hermitian and anti-Hermitian components, $\mathcal{Q}_{ij}(t) = \mathcal{Q}^{s}_{ij}(t) + i\mathcal{Q}^{as}_{ij}(t)$, which can in principle be independently measured[240].

Nondissipative geometric response

The relationship between $\mathcal{Q}_{ij}$ and response functions such as the electric susceptibility $\chi_{ij}(\omega)$ or the electric conductivity $\sigma_{ij}(\omega)$ follows naturally in the geometric picture. Namely, the antisymmetric (in both ij and $\pm\, t$) $\mathcal{Q}^{\mathrm{as}}_{ij}(t) = (\mathcal{Q}_{ij}(t) - \mathcal{Q}_{ji}(-t))/(\mathrm{i})$ is directly related to the polarizability, $\chi(t) = (\pi e^2)\Theta(t)\mathcal{Q}^{as}(t)$[233,240]. Noticing that $J_i(t) = \partial_t p_i(t)$, it follows that the conductivity can be written compactly as[241]

$$\sigma_{ij}(t) \quad = \tfrac{\pi e^2}{\hbar}\Theta(t)\partial_t \mathcal{Q}^{\mathrm{as}}_{ij}(t). \tag{20}$$

which fully reproduces the Kubo formula[236]. We introduce back $\hbar$ explicitly. The two response functions are simply related in the frequency domain by $\sigma_{ij}(\omega) = -i\omega\chi_{ij}(\omega)$. It becomes particularly apparent that for insulators without a Fermi surface, $D_{ij} = 0$, the response at frequencies below the gap, and therefore non-dissipative, is strictly geometric, containing both longitudinal contributions with origin in the interband quantum metric matrix elements, g_{ij}, and Hall contributions from B_{ij}. To make it more apparent, we can expand Eq. (20) for ingap frequencies,

$$\begin{aligned} \sigma_{ij}(\omega) \;=\; & \frac{e^2}{i\hbar}\int_{\mathrm{BZ}} \frac{d^d k}{(2\pi)^d} \sum_{mn} f_{mn\boldsymbol{k}}\left(\left[\mathfrak{g}_{ij}(\boldsymbol{k})\right]_{nm} + \mathrm{i}\left[\mathfrak{b}_{ij}(\boldsymbol{k})\right]_{nm}\right) \\ & \times \left(1 + \omega/\omega_{mn\boldsymbol{k}} + \cdots\right). \end{aligned} \tag{21}$$

Since $f_{mn\boldsymbol{k}} = (f_{n\boldsymbol{k}} - f_{m\boldsymbol{k}})$ is anti-symmetric in band indices, it is apparent that each order in frequency it selects either the symmetric (quantum metric) or antisymmetric (Berry curvature) geometric matrix elements. Namely, in the DC limit, only the Berry curvature contributes. In two dimensions, we obtain the celebrated Thouless-Kohmoto-Nightingale-Nijs formula $\sigma_{ij} = \epsilon_{ij}e^2C/h$[1] with ϵ_{ij} the Levi-Civita symbol. At linear order in ω, the non-dissipative geometric response—the static polarizability, or capacitance of the insulator, χ_{ij}—emerges from the matrix element of the quantum metric weighted by the inverse energy gaps[236]:

$$\sigma_{ij}(\omega) = \frac{e^2}{h}\left(C\epsilon_{ij} + i\omega\chi_{ij} + \cdots\right). \tag{22}$$

Sum rules of dissipative response

In this part, we discuss several sum rule for band insulators. First note that, integrating the conductivity tensor $\sigma_{ij}(\omega)$ over all frequencies (up to ω dependent factors) can realize the instantaneous, $t = 0$, response. This realization leads to a sum rule that relates the integrated quantum metric

$$\mathcal{G}_{ij} = \int_{\mathrm{BZ}} \frac{d^d k}{(2\pi)^d} g_{ij}(\boldsymbol{k}) = \frac{1}{2}\left[\mathcal{Q}_{ij} + \mathcal{Q}_{ji}\right] \tag{23}$$

to the integrated real part of the longitudinal conductivity as

$$\mathrm{Tr}[\mathcal{G}] = \frac{\hbar}{\pi e^2}\int_0^\infty d\omega \sum_i \frac{\mathrm{Re}\left[\sigma_{ii}(\omega)\right]}{\omega}\ , \tag{24}$$

which is now recognized as the Souza-Wilkens-Martin (SWM) sum rule[93]. The quantum geometry can also be found in the static structure factor[233,242,243]

$$S(\boldsymbol{q}) = \frac{1}{2}\sum_{ij} q_i q_j \mathcal{G}_{ij} + \ldots \tag{25}$$

Importantly, dissipation also occurs from the magnetic dipole moment of the medium, leading to Hall response. The simplest example is the Hall counterpart of the SWM sum rule, which is exactly the Kramers-Krönig counterpart of the DC Hall conductivity[244] or the dichroic sum rule[245] which captures the orbital magnetic moment of bound electrons permitted by the Berry curvature[246,247]. Here $\sigma^H_{ij}(\omega) = [\sigma_{ij}(\omega) - \sigma_{ji}(\omega)]/2$.

Let us here present the generalization of these results by utilizing Eq. (20) in ref. 237. Different sum rules can be constructed by weighting different powers η of frequency. Each η captures an instantaneous property of the medium characterizing a given moment of the zero point motion of the ground state, or the various time derivatives of $\mathcal{Q}_{ij}(t)$,

$$\mathcal{S}^\eta_{ij} = \int_0^\infty d\omega\ \frac{\sigma^{\mathrm{abs}}_{ij}(\omega)}{\omega^{1-\eta}} = \frac{\pi e^2}{\hbar}(-i\partial_t)^\eta \mathcal{Q}_{ij}(t)|_{t=0}. \tag{26}$$

The absorptive (or Hermitian) part of the conductivity $\sigma^{\mathrm{abs}}_{ij} = \mathrm{Re}\sigma^L_{ij}(\omega) + i\mathrm{Im}\sigma^H_{ij}(\omega)$ (with $\sigma^L_{ij}(\omega) = [\sigma_{ij}(\omega) + \sigma_{ji}(\omega)]/2$) contains a symmetric and real part due to coupling of $\mathcal{E}_i$ aligned with the dipole moment of the dielectric medium, but also a Hall contribution from the coupling with the magnetic dipole, perpendicular to the field. Importantly in the sum rules $\mathcal{S}^\eta$, the entire $\mathcal{Q}_{ij}$ tensor Eq. (18) appears, not only $\mathcal{Q}^{\mathrm{as}}_{ij}$, and therefore, sum rules are sensitive to geometric quantities absent in nondissipative linear response, such as the integrated quantum metric[93].

Sum rules naturally divide into longitudinal and Hall contributions, where each η-time moment of $\mathcal{Q}_{ij}$ corresponds to a convolution with $\omega^\eta_{mn\boldsymbol{k}}$. In insulators, all moments are given exclusively in terms of geometric matrix elements and explicitly given by

$$\mathcal{S}^\eta_{L,ij} = \frac{\pi e^2}{\hbar}\sum_{nm}\int_{\mathrm{BZ}} \frac{d^d k}{(2\pi)^d} f_{n\boldsymbol{k}}(1 - f_{m\boldsymbol{k}})\left[\mathfrak{g}_{ij}(\boldsymbol{k})\right]_{nm}\omega^\eta_{mn\boldsymbol{k}} \tag{27}$$

and

$$\mathcal{S}^\eta_{H,ij} = \frac{\pi e^2}{\hbar}\sum_{nm}\int_{\mathrm{BZ}} \frac{d^d k}{(2\pi)^d} f_{n\boldsymbol{k}}(1 - f_{m\boldsymbol{k}})\left[\mathfrak{b}_{ij}(\boldsymbol{k})\right]_{nm}\omega^\eta_{mn\boldsymbol{k}}\,. \tag{28}$$

These fluctuation moments reflect various instantaneous properties of bound electrons in periodic lattices[241] and have been dubbed quantum weights in ref. 248. Let us now focus on 2D ($d = 2$), where $\mathcal{G}_{ij}$ has no units. Starting with the zeroth moment of longitudinal fluctuations $\mathcal{S}^0_{L,ij} = \pi e^2/\hbar\mathcal{G}_{ij}$, it captures exactly the integrated quantum metric, which is exactly the SWM sum rule[93]. In Chern insulators or Landau levels, where projected of the position operators in orthogonal directions do not commute, the zeroth moment of Hall fluctuations is nonzero $\mathcal{S}^0_{H,ij} = -(\pi e^2/2h)C\epsilon^{ij}$. At $\eta = 1$, quantifying the speed of the polarization fluctuations is the f-sum rule, defining the total spectral weight, $\mathcal{S}^1_L = \pi e^2 n/2m$; and the dichroic sum rule[245], defining the orbital magnetic moment $\mathcal{S}^1_H = \mu_M$, measured in ref. 249. Shot noise, that is zero temperature current fluctuations appear in the second fluctuation moment $\mathcal{S}^2_L$ and $\mathcal{S}^2_H$[88]. Intriguingly, and also noticed early on[250], metals and insulators don't show remarkably different behavior in current fluctuations $\mathcal{S}^\eta$ with $\eta > 0$. However, $\mathcal{S}^0_L$, proportional to the integrated quantum metric, can qualitatively distinguish the two, completing the effort of Kohn to unambiguously distinguish a metal from an insulator[91].

Spectral transfer and optical bounds

In metals not all $\mathcal{S}^\eta$ are well defined, but we can focus on the well-behaved first moment of the longitudinal response, the f-sum rule $\mathcal{S}^1_L$. This sum rule relates to nondissipative response by expanding the conductivity Eq. (20) to frequencies far above optical transitions, $\sigma_{ij}(\omega) \sim i\omega_p^2/\omega$. Here $\omega_p^2 = 4\pi n e^2/m$[250,251], containing the electron density n and optical mass m. The optical mass is defined by $\mathcal{S}^1_L$, which has a Fermi surface contribution given by the Drude weight D_{ij}, the linear in t part of the $\mathcal{Q}_{ij}(t)$ Eq. (18), and a geometric component from the oscillations in $\mathcal{Q}_{ij}(t)$. Therefore, it is natural to separate the spectral weight into the charge stiffness n/m^* obtained by the dispersion curvature at the Fermi level $\pi e^2 n/m^*_{ij} = D_{ij}$ and a geometric contribution from interband optical transitions, $\pi e^2 n/2m^g_{ij} \equiv \sum' \omega_{mn\boldsymbol{k}}[\mathfrak{g}_{ij}(\boldsymbol{k})]_{nm}$[42,252,253] where $\sum'$ is a shorthand for the sum and prefactor of Eq.(27). Therefore, we have that the optical mass of electrons, defined by the sum rule and therefore indicating the instantaneous mass of electrons (usually the bare electron mass[254]) relates to the Fermi surface electron mass and the geometric mass by

$$\frac{1}{m_{ij}} = \frac{1}{m^*_{ij}} + \frac{1}{m^g_{ij}} \tag{29}$$

The geometric contribution generally makes the electrons lighter at short time scales[255]. In the extreme example of flat bands with nontrivial quantum geometry, in which quantum interference creates a band with $m^* = \infty$, the mass is purely geometric. This means that although semiclassical transport would be dictated by infinitely heavy electrons that do not conduct, at short time scales the electrons behave as if they have their original mass before the quenching of the band dispersion. A consequence, as discussed extensively above, is that electrons may still form a superconducting or excitonic condensate.

The transfer of weight from the Fermi surface mass m^* to the geometric mass m^g can be best appreciated in Fig. 3 where we consider a square lattice tight-binding model and show the evolution of the total spectral weight and optical mass $\mathcal{S}^1_L$. The hoppings are tuned such that the bands evolve smoothly into a Lieb lattice. In this process, the Drude peak gets progressively reduced while the geometric mass is built up to the point that exactly in the Lieb limit, the band is perfectly flat and contributes only to the geometric weight.

By looking at the different geometric responses within a unified framework, some identities become apparent. First, an insulator has a spectral gap E_g, which means the energy differences are bounded by $\omega_{mn\boldsymbol{k}} > E_g/\hbar$. It follows that for $\eta > 0$, $S^\eta_{L,ij} = \sum' \omega^\eta_{mn\boldsymbol{k}}[\mathfrak{g}_{ij}(\boldsymbol{k})]_{nm} \geq (\pi e^2/\hbar^2 V)E^\eta_g \mathcal{G}_{ij}$. Similarly $S^\eta_H \geq (4\pi^2 e^2/\hbar^2)E^\eta_g C$. The signs are reversed for the negative powers of η. Focusing on the $f-$ sum rule $\eta = 1$, we have $\pi e^2 nd/m \geq (\pi e^2/\hbar^2)\mathrm{Tr}\mathcal{G}E_g$, which gives $\hbar^2 nd/m \geq \mathrm{Tr}\mathcal{G}E_g$, where d is the spacial dimension. This fact was pointed out by Kivelson in 1982[256] for 1D insulators.

Combining these results with the trace condition Eq. (2) it can be observed that in the presence of a Chern number, it also holds that the

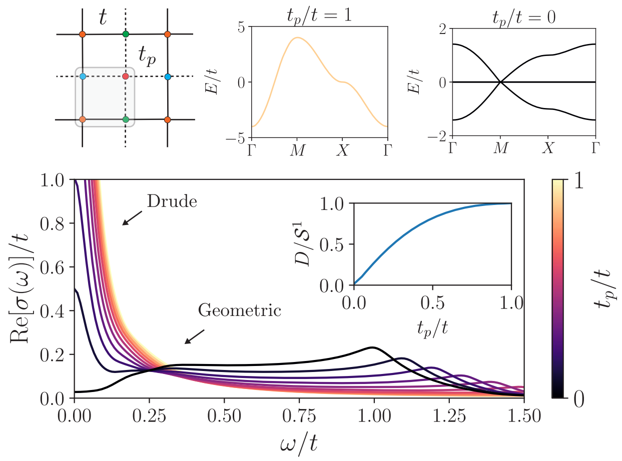

Fig. 3 | Transfer of optical spectral weight Re $\sigma_{xx}(\omega)$ from the Fermi surface (Drude weight) to high frequencies from destructive interference in a frustrated hopping lattice (Lieb). After cutting the hopping t_p, the resulting Hamiltonian has a flat band with no Drude weight, which was distributed to higher energies in the form of dipolar transitions between the flat and dispersive bands.

energy gap is bounded by the inverse Chern number $E_g \leq 2\pi n/(m|C|)$[244]. More optical weight upper and lower bounds have been discussed since focusing on their geometric and topological origins[257,93,235,241,248,258,259,252].

Let us conclude this discussion with the example of free electrons in two dimensions under a magnetic field. From Kohn's theorem[260], Galilean invariance requires that all optical transitions happen exclusively across consecutive Landau levels separated by the cyclotron frequency ω_c. In this case, all sum rules become saturated[258]. In fact, they can be compactly expressed by $\mathcal{S}^{\eta}_{ij} = \frac{\pi e^2}{\hbar} C\omega_c^{\eta}(\delta_{ij} + 2\pi\epsilon_{ij})$ with δ_{ij} the Kronecker delta and ϵ_{ij} the Levi-Civita symbol, which saturates all the bounds[237]. In this case, all responses are quantized, including DC conductivity, capacitance, or magnetic moment. The quantum geometric effect on the optical response was also studied in the presence of correlations[261,262] and various other systems[51,263–267].

Landau levels

Semiclassical quantization of electronic states into Landau levels (LLs) under a magnetic field can be described by the generalized Onsager's rule:

$$S_0(\epsilon) = 2\pi e B\left(n + \tfrac{1}{2} - \tfrac{\gamma_{\epsilon,B}}{2\pi}\right), \tag{30}$$

where $S_0(\epsilon)$ is the momentum space area of the closed semiclassical orbit at the energy ϵ, B is magnetic field,—e is the electron charge, n is a nonnegative integer, and $\gamma_{\epsilon,B}$ is the quantum correction due to Berry phase, magnetic susceptibility, and other band properties[268–272]. The semiclassical approach can successfully describe the band energy and the geometric properties of Bloch states in metallic systems with energy dispersion. This includes free electron gas with parabolic dispersion and Dirac electrons with linear dispersion[5,273]. However, when applied to dispersionless flat bands, the implication of Eq. (30) is subtle since semiclassical orbits are ill-defined. Naively, one may expect vanishing LL spacings due to the infinite effective mass, and thus no response of flat bands to the magnetic field.

However, when a flat band exists in multi-band systems with sizable interband coupling, this naive expectation completely breaks down. Here, the presence of a finite interband coupling indicates that the flat band is not from the decoupled atomic states. In this section, we will first review how the LLs are affected by interband coupling[274]. In particular, we discuss the role of interband Berry connection and symmetry of the system at zero magnetic field on the LL spectra. After that, we discuss the anomalous magnetic responses of singular flat bands in which the flat band has a quadratic band crossing with another parabolic band at which the Bloch wave function becomes singular[275]. The geometric idea to describe the LL of singular flat bands can be further generalized to describe the LL spectra of generic quadratic band crossing[276]. We will discuss the complication when the flat band is made to be weakly dispersive and explain how the geometric effect can be extracted. Based on it, we revisit the magnetic responses of the Bernal stacked bilayer graphene[277].

Isolated flat bands

The Landau level spread of isolated single flat bands can be described by using the *modified semiclassical approach* developed by M.-C. Chang and Q. Niu[278]. Contrary to Onsager's approach, where the band structure at zero magnetic field $\epsilon_{n\boldsymbol{k}}$ is used to define the closed semiclassical orbits and the corresponding area $S_0(\epsilon)$, the modified semiclassical approach[278] employs the modified band structure given by

$$E_{n,B}(\boldsymbol{k}) = \epsilon_{n\boldsymbol{k}} + \mu_n(\boldsymbol{k})B, \tag{31}$$

where $\boldsymbol{B} = B\hat{z}$ is the magnetic field, n is the band index, and $\mu_n(\boldsymbol{k})$ is the orbital magnetic moment of the n-th magnetic band in the z-direction whose explicit form is

$$\mu_n(\boldsymbol{k}) = e\,\mathrm{Im}\left\langle \partial_x u_n(\boldsymbol{k})\right| \left[\epsilon_{n\boldsymbol{k}} - H(\boldsymbol{k})\right] \left|\partial_y u_n(\boldsymbol{k})\right\rangle, \tag{32}$$

where $H(\boldsymbol{k})$ is the matrix Hamiltonian in momentum space. Hence, the second term on the right-hand side of Eq. (31) indicates the leading energy correction from the orbital magnetic moment coupled to the magnetic field. In usual dispersive bands, the B-linear quantum correction is negligibly small in weak magnetic field limit compared to the zero-field bandwidth.

In the case of a flat band with zero bandwidth, on the other hand, the B-linear quantum correction always dominates the modified band structure $E_{n,B}(\boldsymbol{k})$ in Eq. (31) even in weak magnetic field limit. Moreover, the modified band dispersion of an isolated flat band is generally dispersive so that the relevant semiclassical orbits can be defined unambiguously. As a result, one can obtain the LL spreading of the isolated flat band in the adjacent gapped regions by applying the semiclassical quantization rule to $E_{n,B}(\boldsymbol{k})$, which naturally explains the LL spread of the isolated flat band. Especially, around the band edges of $E_{n,B}(\boldsymbol{k})$, one can define the effective mass m^*, which is inversely proportional to B, from which Onsager's scheme predicts Landau levels with a spacing $eB/m^* \propto B^2$. The resulting LL spectrum is bounded by the upper and lower band edges of $E_{n,B}(\boldsymbol{k})$, and thus the total magnitude Δ of the LL spread is given by $\Delta = \max E_{n,B}(\boldsymbol{k}) - \min E_{n,B}(\boldsymbol{k})$. This result is valid as long as the band gap E_{gap} between the isolated flat band and its neighboring band at zero magnetic field is large enough, i.e., $E_{\mathrm{gap}} \gg \max|E_{n,B}(\boldsymbol{k})|$. The generic behavior of an isolated flat band under a magnetic field is schematically described in Fig. 4 where one can clearly observe that the LL spread of the isolated flat band start filling the gaps at zero-field above and below the isolated flat band.

Interestingly, the LL spreading of isolated flat bands is a manifestation of the non-trivial wave function geometry of the flat band arising from interband couplings[274]. One can show that the modified band dispersion of the isolated flat band is given by

$$E_{n,B}(\boldsymbol{k}) = -2\pi\frac{\phi}{\phi_0}\frac{1}{A_0}\mathrm{Im}\sum_{m\neq n}\epsilon_{m\boldsymbol{k}}\chi^{nm}_{xy}(\boldsymbol{k}), \tag{33}$$

in which

$$\begin{aligned}\chi^{nm}_{ij}(\boldsymbol{k}) &= \langle\partial_i u_n(\boldsymbol{k})|u_m(\boldsymbol{k})\rangle\langle u_m(\boldsymbol{k})|\partial_j u_n(\boldsymbol{k})\rangle\\ &= [A_i(\boldsymbol{k})]^*_{mn}[A_j(\boldsymbol{k})]_{mn},\end{aligned} \tag{34}$$

where $\phi_0 = h/e$, $\phi = BA_0$ is the magnetic flux per unit cell, and A_0 is the unit cell area assumed to be $A_0 = 1$. Here, we assume that the n-th band is the isolated flat band at zero energy without loss of generality so that $\epsilon_{m\boldsymbol{k}}$ in Eq. (33) should be interpreted as the energy of the m-th band with respect to the flat

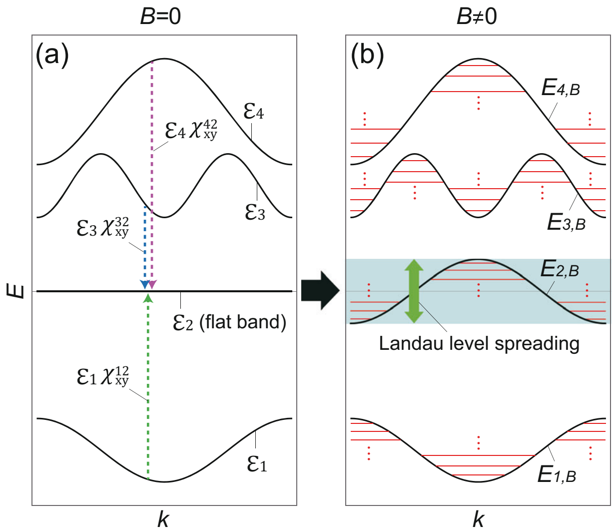

Fig. 4 | Landau level spread of an isolated flat band. a The band structure of a 2D system in the absence of a magnetic field. The second band with the energy $\varepsilon_2 = 0$ corresponds to the isolated flat band. The inter-band coupling $\varepsilon_m\chi^{m2}_{xy}$ of the isolated flat band with the other dispersive band of the energy ε_m ($m = 1, 3, 4$) is indicated by a dashed vertical arrow. **b** The modified band dispersion $E_{m,B}$ ($m = 1, \ldots, 4$) in the presence of the magnetic field. The corresponding Landau levels are shown by red solid lines. The LL spread of the isolated flat band is represented by the green arrow. [Adapted from ref. 274].

band energy. We note that $[A_i(\boldsymbol{k})]_{nm} = \mathrm{i}\langle u_m(\boldsymbol{k})|\partial_i u_n(\boldsymbol{k})\rangle$ indicates the cross-gap Berry connection between the n-th and m-th bands ($n \neq m$), and $\chi^{nm}_{ij}(\boldsymbol{k})$ is the corresponding fidelity tensor that describes the transition amplitude between the n-th and m-th bands. We note that $[A_i(\boldsymbol{k})]_{nm}$ is gauge-covariant while $\chi^{nm}_{ij}(\boldsymbol{k})$ is gauge-invariant, thus directly related to physical observables. Hence, Eq. (33) indicates that the modified band dispersion of the isolated flat band is given by the summation of the transition amplitudes $\chi^{nm}_{xy}(\boldsymbol{k})$ between the isolated flat band and the m-th band weighted by the energy $\epsilon_{m\boldsymbol{k}}$ of the m-th band as illustrated in Fig. 4. This means that the immobile carriers with infinite effective mass in an isolated flat band can respond to the external magnetic field through the inter-band coupling, characterized by the cross-gap Berry connection, to dispersive bands.

The LL spread of an isolated flat band is strongly constrained by the symmetry group of the system[274]. The B-linear correction to the modified band dispersion $E_{n,B}(\boldsymbol{k})$ vanishes when the system respects the chiral C or space-time-inversion I_{ST} symmetries in the zero magnetic flux. The LL spreading is proportional to B^2 for a flat-band system with I_{ST} symmetry in the zero magnetic field, while the LL spreading is forbidden in the presence of chiral symmetry. Interestingly, although I_{ST} symmetry would be broken as the magnetic field is turned on, the LL spreading is strongly constrained by I_{ST} symmetry. We further find that $\max E_{n,B}(\boldsymbol{k}) = -\min E_{n,B}(\boldsymbol{k})$ when the system respects time-reversal T or reflection R symmetry, at the zero magnetic field, thus the minimum and maximum values of the LL spreading have the same magnitude but with the opposite signs.

Singular flat band with quadratic touching

Next, let us consider the LL spectrum of singular flat bands in which a flat band has a band crossing with other dispersive bands at a momentum where the flat band wave function develops a singularity[279–281]. As a minimal model of a singular flat band, we consider a two-band model describing a flat band crossing quadratically with a parabolic band. Explicitly, we consider the most general form of two-band continuum quadratic Hamiltonian given by

$$\mathcal{H}_Q(\mathbf{k}) \equiv f_0(\mathbf{k})\sigma_0 + \sum_{\alpha=x,y,z} f_\alpha(\mathbf{k})\sigma_\alpha, \tag{35}$$

where σ_α's are Pauli matrices and σ_0 is the 2×2 identity matrix. The quadratic functions $f_{\alpha=0,x,y,z}(\boldsymbol{k})$ take the form of $f_\alpha(\mathbf{k}) = a_\alpha k_x^2 + b_\alpha k_x k_y + c_\alpha k_y^2$ with real coefficients $\{a_\alpha, b_\alpha, c_\alpha\}$. A flat band touching with another parabolic band can be obtained by imposing the band flatness condition $\det[\mathcal{H}_Q(\mathbf{k})] = 0$. If the resulting flat band wave function develops discontinuity at the band crossing point, we obtain a singular flat band. Otherwise, we have a non-singular flat band.

The singular band crossing point can be characterized by the canting structure of the pseudospin $\mathbf{s}(\mathbf{k}) \equiv \sum_{\alpha=x,y,z} f_\alpha(\mathbf{k})/\sqrt{f_x(\mathbf{k})^2 + f_y(\mathbf{k})^2 + f_z(\mathbf{k})^2}\,\hat{\alpha}$ around the band crossing point. The canting structure arises due to the singularity at the band crossing point where the pseudospin direction cannot be uniquely determined. The strength of the singularity can be characterized by the maximum canting angle $\Delta\theta_{\max}$ of the pseudospin around the band crossing point. Interestingly, the canting angle between two pseudospins at the momenta $\mathbf{k}, \mathbf{k}'$ is related to the Hilbert-Schmidt quantum distance $d_{\mathrm{HS}}(\mathbf{k}, \mathbf{k}') \equiv \sqrt{1 - |\langle u_{\mathbf{k}}|u_{\mathbf{k}'}\rangle|^2}$ of the perodic parts of the relevant Bloch states $|u_{\mathbf{k}}\rangle$, $|u_{\mathbf{k}'}\rangle$ as $\Delta\theta(\mathbf{k}, \mathbf{k}') = 2\sin^{-1}(d_{\mathrm{HS}}(\mathbf{k}, \mathbf{k}'))$. Denoting the maximum value of d_{HS} as $d_{\max}$ gives $\Delta\theta_{\max} = 2\sin^{-1}(d_{\max})$. So, either $\Delta\theta_{\max}$ or $d_{\max}$ can equivalently measure the strength of the singularity[275]. In the perspective of the quantum distance, the singularity at the band crossing point prevents Bloch wave functions from getting close to each other even in the limit $\mathbf{k} \to 0$ yielding nonzero $d_{\max}$.

A singular flat band under a magnetic field develops an anomalous LL structure, which directly manifests the quantum geometry of the wave function associated with the singularity at the band crossing point[275–277]. Figure 5b, c show the generic LL spectra of a non-singular flat band and a singular flat band, obtained by solving Eq. (35) under magnetic field. One can see that the non-singular flat band does not respond to the magnetic field, and all of its LL states are located at the same energy (that of the zero field flat band) without any spread. On the other hand, the singular flat band develops its LL spreading in the *empty region* (i.e., with energy below that of the flat band). In both cases, the parabolic band develops a conventional LL structure with equal energy spacing ω_c.

One can define the total LL spread Δ of the singular flat band as the difference between the energy of the singular flat band and that of the lowest LL (E_0) assuming that the flat band has lower energy than the parabolic band. One striking observation[275] is that there is a universal relationship between Δ/ω_c and $d_{\max}$, independent of model parameters used to define the quadratic Hamiltonian in Eq. (35), given by

$$\frac{\Delta}{\omega_c} = \xi(d^2_{\max}), \tag{36}$$

where $\xi(x)$ is a monotonically increasing curve shown in Fig. 5e. The existence of the universal function $\xi(x)$ can be proved analytically as well as numerically. Therefore, measuring Δ/ω_c, $d_{\max}$ of the singular flat band can be experimentally extracted. Eq. (36) implies that Δ/ω_c is determined solely by $d_{\max}$, and the LL spreading of singular flat bands is characterized by two distinct energy scales Δ and ω_c, contrary to the case of non-singular flat band with just one energy scale ω_c. Describing the LL generation of singular flat bands in the empty region is completely beyond the scope of semiclassical analysis, arising from the level repulsion between the LL spreading from the singular flat band and those from the parabolic band, which is encoded in the maximum quantum distance.

Quadratic band crossing and bilayer graphene

Now we relax the flat band condition and consider the LL spectrum of a general two-band quadratic band crossing Hamiltonian $\mathcal{H}_Q(\mathbf{k})$ in Eq. (35) with $f_{\alpha=0,x,y,z}(\mathbf{k}) = a_\alpha k_x^2 + b_\alpha k_x k_y + c_\alpha k_y^2$. After a series of unitary

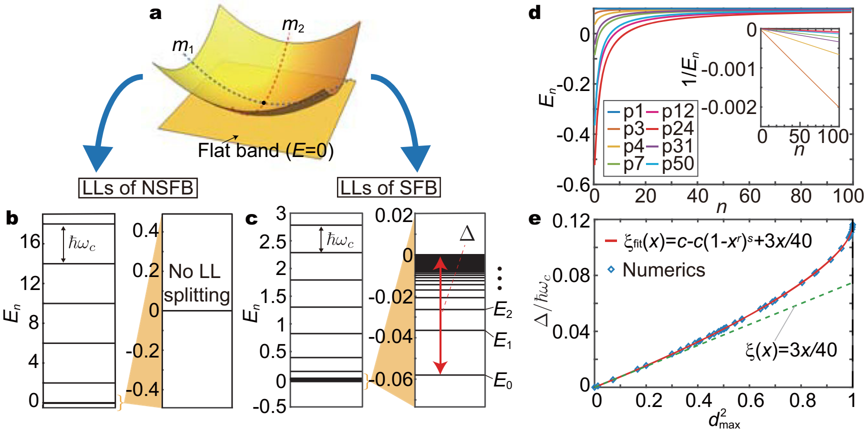

Fig. 5 | Landau level spectrum of a singular flat band. **a** The band structure of a flat band with a quadratic band-crossing. Here m_1 and m_2 are the maximum and minimum effective masses of the dispersive band. **b** and **c** show the LL spreading for a non-singular flat band (NSFB) and singular flat band (SFB), respectively. **d** LL spreading of various flat band models (denoted by the labeling $[pm]$ with an integer m in the inset) as functions of the LL index n. Inset shows their $1/n$ dependences for $n \gg 1$. **e** The universal relationship between Δ/ω_c and $d_{\rm max}$. Numerical data (diamond symbols) are from the 50 flat band models. [Adapted from ref. 275].

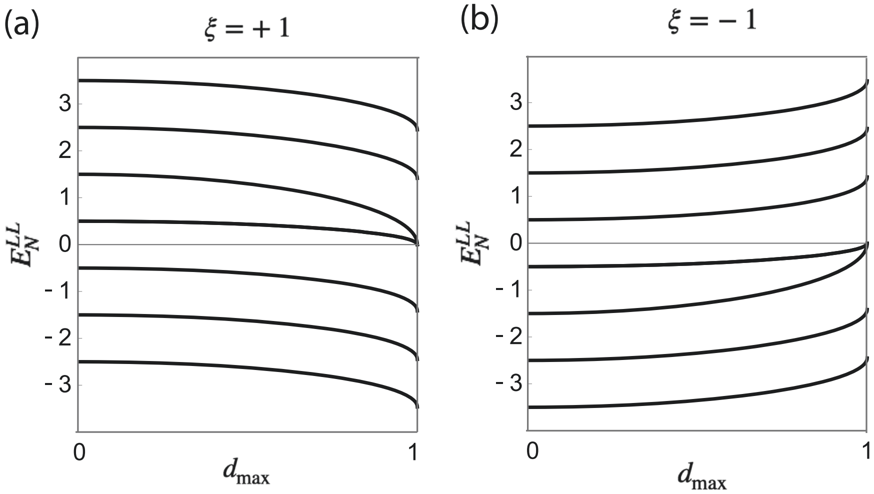

Fig. 6 | Effect of quantum distance on Landau levels. The evolution of the Landau levels E_N^{LL} of a quadratic band crossing Hamiltonian in Eq. (38) as a function of the maximum quantum distance $d_{\rm max}$ for **a** $\xi = +1$ and **b** $\xi = -1$, respectively, with $\omega = 1$. Here, $\xi = \pm 1$ is related to the valley index of graphene. [Adapted from ref. 277].

transformations, the Hamiltonian can be transformed to

$$\begin{aligned} H_Q(\boldsymbol{k}) &= [q_1(k_x^2+k_y^2)+q_2(k_x^2-k_y^2)+q_3(2k_xk_y)]\sigma_0 \\ &\quad +[b_2(k_x^2-k_y^2)+b_3(2k_xk_y)]\sigma_1+[c_3(2k_xk_y)]\sigma_2 \\ &\quad +[a_1(k_x^2+k_y^2)+a_2(k_x^2-k_y^2)+a_3(2k_xk_y)]\sigma_3, \end{aligned} \tag{37}$$

thus, the number of the Hamiltonian parameters reduced from twelve to nine[279]. Interestingly, among the nine parameters, six correspond to the mass tensors of the two dispersive quadratic bands, while the other three describe the interband coupling[275], meaning that the two parabolic bands are from decoupled atomic states in the absence of the interband coupling. In particular, considering that the wave function geometry of $\mathcal{H}_Q(\mathbf{k})$ appears in the form of an elliptic shape on the Bloch sphere, the three interband coupling parameters determine the major d_1 and minor d_2 diameters of the elliptic curve and the orientation of the ellipse represented by an angular variable ϕ[276,282]. When the flat band condition is additionally imposed in a way that one of the two bands becomes flat since it generates five constraint equations among the nine parameters, only four of them become independent and correspond to the three mass tensors of the parabolic band and one interband coupling parameter, which is nothing but the maximum quantum distance[275].

Moreover, one can show that the flat band condition is nothing but the condition that the energy eigenvalues of the two-band Hamiltonian have a quadratic analytic form[276]. Under such quadratic form condition, the generic two-band Hamiltonian has only one interband coupling parameter, which is equivalent to the maximum quantum distance, and the corresponding wave function trajectory on the Bloch sphere is a circle whose diameter is equal to the maximum quantum distance[276,282].

The LL spectrum of generic two-band quadratic band crossing Hamiltonians is also significantly influenced by the three interband coupling parameters. One can reveal the role of the interband coupling in the LL spectrum by comparing two quadratic bands with identical mass tensors but different interband couplings[276]. To demonstrate the role of the interband coupling in the LL spectrum of quadratic band crossing Hamiltonian, let us consider the following model Hamiltonian[277],

$$\mathcal{H}_0(\boldsymbol{k}) = \sum_{\alpha=0,x,y,z} f_\alpha(\boldsymbol{k})\sigma_\alpha, \tag{38}$$

where $f_z(\boldsymbol{k}) = -d\sqrt{1-d^2}k_y^2$, $f_y(\boldsymbol{k}) = d\,k_xk_y$, $f_x(\boldsymbol{k}) = k_x^2/2+(1-2d^2)k_y^2/2$, and $f_0(\boldsymbol{k}) = 0$. Here, the parameter d is defined as $d = \xi d_{\rm max}$ in which $\xi = \pm 1$, and $d_{\rm max}$ is the maximum quantum distance. The energy eigenvalues of $\mathcal{H}_0(\boldsymbol{k})$ remain fixed to be $\epsilon_{\pm,\boldsymbol{k}} = \pm\frac{1}{2}(k_x^2+k_y^2)$ regardless of the value of d within the range $-1 \le d \le 1$. When $d_{\rm max} = 1$, the Hamiltonian in Eq. (38) corresponds to the low energy Hamiltonian of the Bernal stacked bilayer graphene, and $\xi = \pm 1$ denotes the valley index.

In Fig. 6, the $d_{\rm max}$-dependence of LLs is depicted[277]. When $d_{\rm max} = 0$, the LLs E_N^{LL} are equivalent to those of the conventional parabolic bands $\epsilon_N^{\rm conv} = \pm\omega(N+\frac{1}{2})$ with the cyclotron frequency $\omega = eB/m$ but start to deviate from $\epsilon_N^{\rm conv}$ as $d_{\rm max}$ increases. When $d_{\rm max}$ reaches one, they become $\epsilon_N^{\rm bilayer} = \pm\omega\sqrt{N(N-1)}$, the LL of the bilayer graphene. The degeneracy of LLs between $E_0^{LL}(d_{\max}=1)$ and $E_1^{LL}(d_{\max}=1)$ leads to the absence of a zero energy plateau in the quantum Hall effect. Since such degeneracy of LLs occurs only when $d_{\max}=1$, the zero energy plateau is absent only when $d_{\max}=1$ while it exists in other cases with $d_{\max}\neq 1$[277].

One can verify that the degeneracy at $d_{\max}=1$ exists for both $\xi=\pm 1$. However, depending on ξ, the origin of zero LLs is different[277]. For $\xi=+1$, the two zero energy levels come from the upper band, while for $\xi=-1$, the two zero energy levels come from the lower band. Furthermore, when $d_{\max}=1$ or $d_{\max}=0$, the LLs are symmetric with respect to $E=0$, as shown in Fig. 6a, b. This result arises from chiral symmetry, represented by the operator σ_z, which satisfies $\sigma_z H_0(\boldsymbol{k})\sigma_z=-H_0(\boldsymbol{k})$, exclusively when $d_{\max}=1$ or $d_{\max}=0$. This symmetry holds even in the presence of a magnetic field. In fact, the chiral symmetry is crucial for the degeneracy observed at $d_{\max}=1$. Thus, the presence of the zero energy plateau necessitates chiral symmetry as well as $d_{\max}=1$. It is worth noting that although chiral symmetry is not crystalline but approximate symmetry[283], it is an excellent symmetry of bilayer graphene, and thus the absence of the zero energy plateau can be experimentally demonstrated[284].

Outlook

The exploration of quantum geometry in condensed matter physics is in its early stages, with many avenues for further research (see ref. 65). While the equilibrium behavior of quantum geometric superconductivity under assumed attractive interactions is fairly well understood, simple analytical results are mainly confined to the isolated flat band limit. A significant challenge is that interactions in real materials are predominantly repulsive due to Coulomb forces, making ferromagnetism the primary instability in flat bands with quantum geometry. This is evident in kagome metals[285], where most systems become ferromagnetic despite the presence of flat bands at the Fermi level, with only one known low-temperature superconductor.

Further research is needed to identify conditions (if any) where flat-band superconductivity is favored over flat-band ferromagnetism, extending beyond current models. Numerical studies show that superconductivity with purely attractive interactions is enhanced by nearby bands adjacent to flat bands[59,98,108,286]. Analytical insights into non-isolated flat bands and especially repulsive interactions would be highly beneficial. Additionally, understanding how flat bands and quantum geometry affect various superconducting phenomena—such as critical currents, coherence lengths, vortex properties, Josephson junctions, Andreev reflections, and non-equilibrium responses—is crucial. While research in these areas is still emerging[113–115,117–119,287], early indications suggest that flat-band quantum geometric superconductivity could offer new functionalities like devices with suppressed quasiparticle currents[124]. However, definitive experiments and proposals are still lacking, and most current evidence remains circumstantial.

The exploration of quantum geometry in non-equilibrium phenomena should extend beyond superconductivity to include non-Hermitian systems. Collaborations between condensed matter physics and photonic or artificial quantum systems are particularly promising[288–291]. Several experimental observations of the QGT have been reported in the latter systems[292–296]. Connecting current knowledge on quantum geometric effects in superconductivity and Bose-Einstein condensates via BCS-BEC crossover studies[116] would be valuable. To fully grasp the significance of quantum geometry on correlated states, additional experiments and thorough theoretical analyses using realistic models are necessary. Notably, recent experiments have begun exploring quantum geometric effects in TBG superconductivity[66,297], although the extent to which flat band quantum geometry or other, renormalized bands contribute to the physics is unknown. Exploring the effect of quantum geometry in unconventional magentism is also a worthy direction[298]. In fractional Chern insulators[83,185–191,212–215], it is expected that both the Berry curvature and quantum geometry will lead to new effects, but a clear theoretical demonstration of this and an experimental observation are missing. Additionally, the first direct observations of quantum geometric quantities in solid-state systems are emerging[299–301] (albeit[299] in an ionic system).

To expand the impact of quantum geometry in materials research, a key challenge is to define, extract, and apply quantum geometric concepts in ab initio calculations and machine learning methods. These concepts are already utilized in the Wannier approach to electronic structures, serving as indicators for Wannier spread. However, dealing with entangled bands requires addressing issues like divergences in the QGT due to band touchings and extracting QGT from numerical Green's functions. Expanding the range of quantum geometric tools beyond the QGT—such as incorporating quantum distance or the real-space-local quantum metric[45,110,167]-may be necessary.

It is important to note that the QGT is a embedding-dependent quantity[99]; in the case of Bloch states, it depends on Fourier transformation conventions. While some physical observables are embedding-dependent and can be proportional to the QGT, others are embedding-independent and cannot. For instance, the superfluid weight is proportional to the *minimal* quantum metric[98], which resolves this issue. Embedding-independent measures like quantum distance and the real-space-local quantum metric[45,110,167] suggest that new, physically relevant quantum geometric quantities remain to be discovered. Furthermore, we would like to mention that the geometric properties of Bloch states are not completely captured by the QGT. In general, all gauge-invariant properties of the Bloch states fall under the concept of quantum geometry. Therefore, finding new quantities that can capture physically-relevant geometric information beyond QGT, such as the orbital-selective quantum metric in[110,167], is one interesting and important future direction.

This review highlighted the role of the single-particle QGT in condensed matter physics, focusing on the geometric properties of the Bloch states. Remarkably, properties of many-body systems—even those that are strongly interacting—can often be described approximately, and sometimes exactly[59,98,104,302,303], using the easily computed single-particle QGT. Looking forward, it is promising to explore the physical significance of many-body quantum geometry. For example, the many-body QGT has been predicted to provide a bound on the Drude weight in gapped systems[304] and to characterize many-body localization[305]. Recent works demonstrate the relation between many-body quantum geometry and entanglement[306,307], which means many-body QGT could become valuable in characterizing highly correlated quantum materials where mean-field approaches fail, where the many-body QGT is calculated for many-body states by reinterprating $\boldsymbol{k}$ in Eq. (6) as the phase of the twisted boundary condition. In this context, calculating the many-body QGT and other quantum geometric quantities using current and future quantum computers[308,309] is important. In summary, quantum geometry has garnered significant attention[310–315], and its study is expected to yield more interesting results within and beyond condensed matter physics in the future.

Data availability

No datasets were generated or analysed during the current study.

Received: 14 March 2025; Accepted: 4 July 2025;

References

1. Thouless, D. J., Kohmoto, M., Nightingale, M. P. & den Nijs, M. Quantized Hall conductance in a two-dimensional periodic potential. *Phys. Rev. Lett.* **49**, 405–408 (1982).
2. Provost, J. P. & Vallee, G. Riemannian structure on manifolds of quantum states. *Commun. Math. Phys.* **76**, 289–301 (1980).
3. Fubini, G. Sulle metriche definite da una forma hermitiana. *Atti Ist. Veneto* **63**, 502 (1904).
4. Study, E. Kürzeste Wege im komplexen Gebiet. *Math. Ann.* **60**, 321–378 (1905).

5. Berry, M. V. Quantal phase factors accompanying adiabatic changes. *Proc. R. Soc. Lond. A Math. Phys. Sci.* **392**, 45–57 (1984).
6. Simon, B. Holonomy, the quantum adiabatic theorem, and Berry's phase. *Phys. Rev. Lett.* **51**, 2167–2170 (1983).
7. Aharonov, Y. & Anandan, J. Phase change during a cyclic quantum evolution. *Phys. Rev. Lett.* **58**, 1593–1596 (1987).
8. Roy, R. Band geometry of fractional topological insulators. *Phys. Rev. B* **90**, 165139 (2014).
9. Bellissard, J., van Elst, A. & Schulz Baldes, H. The noncommutative geometry of the quantum Hall effect. *J. Math. Phys.* **35**, 5373–5451 (1994).
10. Xie, F., Song, Z., Lian, B. & Bernevig, B. A. Topology-bounded superfluid weight in twisted bilayer graphene. *Phys. Rev. Lett.* **124**, 167002 (2020).
11. Yu, J., Xie, M., Wu, F. & Das Sarma, S. Euler-obstructed nematic nodal superconductivity in twisted bilayer graphene. *Phys. Rev. B* **107**, L201106 (2023).
12. Kwon, S. & Yang, B.-J. Quantum geometric bound and ideal condition for Euler band topology. *Phys. Rev. B* **109**, L161111 (2024).
13. Jankowski, W. J., Morris, A. S., Bouhon, A., šnal, F. N. & Slager, R.-J. Optical manifestations and bounds of topological Euler class. *Phys. Rev. B* **111**, L081103 (2025).
14. Herzog-Arbeitman, J., Peri, V., Schindler, F., Huber, S. D. & Bernevig, B. A. Superfluid weight bounds from symmetry and quantum geometry in flat bands. *Phys. Rev. Lett.* **128**, 087002 (2022).
15. Tovmasyan, M., Peotta, S., Törmä, P. & Huber, S. D. Effective theory and emergent SU(2) symmetry in the flat bands of attractive hubbard models. *Phys. Rev. B* **94**, 245149 (2016).
16. Yu, J., Herzog-Arbeitman, J. & Bernevig, B. A. Universal Wilson loop Bound of Quantum Geometry: Z_2 Bound and Physical Consequences. *arXiv* https://arxiv.org/abs/2501.00100 (2024).
17. Kane, C. L. & Mele, E. J. Z_2 topological order and the quantum spin Hall effect. *Phys. Rev. Lett.* **95**, 146802 (2005).
18. Bernevig, B. A. & Zhang, S.-C. Quantum spin Hall effect. *Phys. Rev. Lett.* **96**, 106802 (2006).
19. Kane, C. L. & Mele, E. J. Quantum spin Hall effect in graphene. *Phys. Rev. Lett.* **95**, 226801 (2005).
20. Bernevig, B. A., Hughes, T. L. & Zhang, S.-C. Quantum spin Hall effect and topological phase transition in hgte quantum wells. *Science* **314**, 1757–1761 (2006).
21. Hasan, M. Z. & Kane, C. L. *Colloquium*: topological insulators. *Rev. Mod. Phys.* **82**, 3045–3067 (2010).
22. Qi, X.-L. & Zhang, S.-C. Topological insulators and superconductors. *Rev. Mod. Phys.* **83**, 1057–1110 (2011).
23. Chiu, C.-K., Teo, J. C. Y., Schnyder, A. P. & Ryu, S. Classification of topological quantum matter with symmetries. *Rev. Mod. Phys.* **88**, 035005 (2016).
24. Vafek, O. & Vishwanath, A. Dirac fermions in solids: from high-T c cuprates and graphene to topological insulators and Weyl semimetals. *Annu Rev. Condens. Matter Phys.* **5**, 83–112 (2014).
25. Wehling, T., Black-Schaffer, A. & Balatsky, A. Dirac materials. *Adv. Phys.* **63**, 1–76 (2014).
26. Burkov, A. Weyl metals. *Annu. Rev. Condens. Matter Phys.* **9**, 359–378 (2018).
27. Benalcazar, W. A., Bernevig, B. A. & Hughes, T. L. Quantized electric multipole insulators. *Science* **357**, 61–66 (2017).
28. Schindler, F. et al. Higher-order topological insulators. *Sci. Adv.* **4**, eaat0346 (2018).
29. Song, Z., Fang, Z. & Fang, C. Dimensional edge states of rotation symmetry protected topological states. *Phys. Rev. Lett.* **119**, 246402 (2017).
30. Khalaf, E. Higher-order topological insulators and superconductors protected by inversion symmetry. *Phys. Rev. B* **97**, 205136 (2018).
31. Ezawa, M. Minimal models for Wannier-type higher-order topological insulators and phosphorene. *Phys. Rev. B* **98**, 045125 (2018).
32. Trifunovic, L. & Brouwer, P. W. Higher-order bulk-boundary correspondence for topological crystalline phases. *Phys. Rev. X* **9**, 011012 (2019).
33. Avron, J. E., Seiler, R. & Zograf, P. G. Viscosity of quantum Hall fluids. *Phys. Rev. Lett.* **75**, 697–700 (1995).
34. Read, N. Non-Abelian adiabatic statistics and Hall viscosity in quantum Hall states and px + ipy paired superfluids. *Phys. Rev. B* **79**, 045308 (2009).
35. Haldane, F. D. M. "Hall viscosity" and intrinsic metric of incompressible fractional Hall fluids. arXiv: 0906.1854 (2009).
36. Read, N. & Rezayi, E. H. Hall viscosity, orbital spin, and geometry: paired superfluids and quantum Hall systems. *Phys. Rev. B* **84**, 085316 (2011).
37. Hoyos, C. & Son, D. T. Hall viscosity and electromagnetic response. *Phys. Rev. Lett.* **108**, 066805 (2012).
38. Bradlyn, B., Goldstein, M. & Read, N. Kubo formulas for viscosity: Hall viscosity, Ward identities, and the relation with conductivity. *Phys. Rev. B* **86**, 245309 (2012).
39. Haldane, F. D. M. & Shen, Y. Geometry of Landau orbits in the absence of rotational symmetry. arXiv: 1512.04502 (2015).
40. Shapourian, H., Hughes, T. L. & Ryu, S. Viscoelastic response of topological tight-binding models in two and three dimensions. *Phys. Rev. B* **92**, 165131 (2015).
41. Holder, T., Queiroz, R. & Stern, A. Unified description of the classical Hall viscosity. *Phys. Rev. Lett.* **123**, 106801 (2019).
42. Resta, R. The Insulating State of Matter: A Geometrical Theory. in *The physics of correlated insulators, metals, and superconductors, Lecture Notes of the Autumn School on Correlated Electrons* 2017, (eds. Pavarini, E. et al.) https://www.cond-mat.de/events/correl17/manuscripts/correl17.pdf (2017).
43. Gao, Y., Yang, S. A. & Niu, Q. Geometrical effects in orbital magnetic susceptibility. *Phys. Rev. B* **91**, 214405 (2015).
44. Resta, R. Drude weight and superconducting weight. *J. Phys: Condens Matter* **30**, 414001 (2018).
45. Marrazzo, A. & Resta, R. Local theory of the insulating state. *Phys. Rev. Lett.* **122**, 166602 (2019).
46. Bellomia, G. & Resta, R. Drude weight in systems with open boundary conditions. *Phys. Rev. B* **102**, 205123 (2020).
47. Gao, Y., Yang, S. A. & Niu, Q. Field induced positional shift of Bloch electrons and its dynamical implications. *Phys. Rev. Lett.* **112**, 166601 (2014).
48. Morimoto, T. & Nagaosa, N. Topological nature of nonlinear optical effects in solids. *Sci. Adv.* **2**, e1501524 (2016).
49. Nagaosa, N. & Morimoto, T. Concept of quantum geometry in optoelectronic processes in solids: application to solar cells. *Adv. Mater.* **29**, 1603345 (2017).
50. Kolodrubetz, M., Sels, D., Mehta, P. & Polkovnikov, A. Geometry and non-adiabatic response in quantum and classical systems. *Phys. Rep.* **697**, 1–87 (2017).
51. Ahn, J., Guo, G.-Y. & Nagaosa, N. Low-frequency divergence and quantum geometry of the bulk photovoltaic effect in topological semimetals. *Phys. Rev. X* **10**, 041041 (2020).
52. Ahn, J., Guo, G.-Y., Nagaosa, N. & Vishwanath, A. Riemannian geometry of resonant optical responses. *Nat. Phys.* **18**, 290–295 (2022).
53. Wang, C., Gao, Y. & Xiao, D. Intrinsic nonlinear Hall effect in antiferromagnetic tetragonal CuMnAs. *Phys. Rev. Lett.* **127**, 277201 (2021).
54. Ma, D., Arora, A., Vignale, G. & Song, J. C. W. Anomalous skew-scattering nonlinear Hall effect and chiral photocurrents in PT-symmetric antiferromagnets. *Phys. Rev. Lett* **131**, 076601 (2023).
55. Liu, T., Qiang, X.-B., Lu, H.-Z. & Xie, X. C. Quantum geometry in condensed matter. *Natl. Sci. Rev.* **12**, nwae334 (2024).
56. Avdoshkin, A., Mitscherling, J. & Moore, J. E. The multi-state geometry of shift current and polarization. arXiv: 2409.16358 (2024).

57. Sala, G. et al. The quantum metric of electrons with spin-momentum locking. arXiv: 2407.06659 (2024).
58. Peotta, S. & Törmä, P. Superfluidity in topologically nontrivial flat bands. *Nat. Commun.* **6**, 8944 (2015).
59. Julku, A., Peotta, S., Vanhala, T. I., Kim, D.-H. & Törmä, P. Geometric origin of superfluidity in the Lieb-lattice flat band. *Phys. Rev. Lett.* **117**, 045303 (2016).
60. Liang, L. et al. Band geometry, Berry curvature, and superfluid weight. *Phys. Rev. B* **95**, 1–16 (2017).
61. Hu, X., Hyart, T., Pikulin, D. I. & Rossi, E. Geometric and conventional contribution to the superfluid weight in twisted Bilayer graphene. *Phys. Rev. Lett.* **123**, 237002 (2019).
62. Julku, A., Peltonen, T. J., Liang, L., Heikkilä, T. T. & Törmä, P. Superfluid weight and Berezinskii-Kosterlitz-Thouless transition temperature of twisted bilayer graphene. *Phys. Rev. B* **101**, 060505 (2020).
63. Rossi, E. Quantum metric and correlated states in two-dimensional systems. *Curr. Opin. Solid State Mater. Sci.* **25**, 100952 (2021).
64. Törmä, P., Peotta, S. & Bernevig, B. A. Superconductivity, superfluidity and quantum geometry in twisted multilayer systems. *Nat. Rev. Phys.* **4**, 528–542 (2022).
65. Törmä, P. Essay: where can quantum geometry lead us? *Phys. Rev. Lett.* **131**, 240001 (2023).
66. Tian, H. et al. Evidence for Dirac flat band superconductivity enabled by quantum geometry. *Nature* **614**, 440–444 (2023).
67. Cao, Y. et al. Correlated insulator behaviour at half-filling in magic-angle graphene superlattices. *Nature* **556**, 80–84 (2018).
68. Cao, Y. et al. Unconventional superconductivity in magic-angle graphene superlattices. *Nature* **556**, 43–50 (2018).
69. Yankowitz, M. et al. Tuning superconductivity in twisted bilayer graphene. *Science* **363**, 1059–1064 (2019).
70. Chen, G. et al. Signatures of tunable superconductivity in a trilayer graphene moiré superlattice. *Nature* **572**, 215–219 (2019).
71. Lu, X. et al. Superconductors, orbital magnets and correlated states in magic-angle bilayer graphene. *Nature* **574**, 653–657 (2019).
72. Choi, Y. et al. Electronic correlations in twisted bilayer graphene near the magic angle. *Nat. Phys.* **15**, 1174–1180 (2019).
73. Sharpe, A. L. et al. Emergent ferromagnetism near three-quarters filling in twisted bilayer graphene. *Science* **365**, 605–608 (2019).
74. Polshyn, H. et al. Large linear-in-temperature resistivity in twisted bilayer graphene. *Nat. Phys.* **15**, 1011–1016 (2019).
75. Codecido, E. et al. Correlated insulating and superconducting states in twisted bilayer graphene below the magic angle. *Sci. Adv.* **5**, eaaw9770 (2019).
76. Liu, X. et al. Tunable spin-polarized correlated states in twisted double bilayer graphene. *Nature* **583**, 221–225 (2020).
77. Shen, C. et al. Correlated states in twisted double bilayer graphene. *Nat. Phys.* **16**, 520–525 (2020).
78. Chen, G. et al. Tunable correlated Chern insulator and ferromagnetism in a moiré superlattice. *Nature* **579**, 56–61 (2020).
79. Cao, Y. et al. Tunable correlated states and spin-polarized phases in twisted bilayer–bilayer graphene. *Nature* **583**, 215–220 (2020).
80. Andrei, E. Y. & MacDonald, A. H. Graphene bilayers with a twist. *Nat. Mater.* **19**, 1265–1275 (2020).
81. Mao, N. et al. Lattice relaxation, electronic structure and continuum model for twisted bilayer MoTe_2. *Commun. Phys*. **7**, 262 (2024).
82. Dong, J., Wang, J., Ledwith, P. J., Vishwanath, A. & Parker, D. E. Composite fermi liquid at zero magnetic field in twisted MoTe2. *Phys. Rev. Lett*. **131**, 136502 (2023).
83. Redekop, E. et al. Direct magnetic imaging of fractional Chern insulators in twisted MoTe_2 with a superconducting sensor. arXiv: 2405.10269 (2024).
84. Helstrom, C. W.*Quantum Detection and Estimation Theory*. No. v. 123 in Mathematics in Science and Engineering (Academic Press, 1976).
85. Pezzé, L. & Smerzi, A. Entanglement, nonlinear dynamics, and the Heisenberg limit. *Phys. Rev. Lett.* **102**, 100401 (2009).
86. Paris, M. G. A. Quantum estimation for quantum technology. *Int. J. Quantum Inf.* **07**, 125–137 (2009).
87. Bernevig, B. A. & Hughes, T. L.*Topological Insulators and Topological Superconductors* (Princeton University Press, 2013).
88. Neupert, T., Chamon, C. & Mudry, C. Measuring the quantum geometry of Bloch bands with current noise. *Phys. Rev. B* **87**, 245103 (2013).
89. Fertig, H. A. & Brey, L. Many-body quantum geometric dipole. arXiv: 2406.12089 (2024).
90. Blount, E. *Formalisms of Band Theory* (Academic Press, 1962).
91. Kohn, W. Theory of the insulating state. *Phys. Rev.* **133**, A171–A181 (1964).
92. Resta, R. & Sorella, S. Electron localization in the insulating state. *Phys. Rev. Lett.* **82**, 370–373 (1999).
93. Souza, I., Wilkens, T. & Martin, R. M. Polarization and localization in insulators: generating function approach. *Phys. Rev. B* **62**, 1666–1683 (1999).
94. Marzari, N., Mostofi, A. A., Yates, J. R., Souza, I. & Vanderbilt, D. Maximally localized wannier functions: theory and applications. *Rev. Mod. Phys.* **84**, 1419–1475 (2012).
95. Marzari, N. & Vanderbilt, D. Maximally localized generalized Wannier functions for composite energy bands. *Phys. Rev. B* **56**, 12847–12865 (1997).
96. Brouder, C., Panati, G., Calandra, M., Mourougane, C. & Marzari, N. Exponential localization of Wannier functions in insulators. *Phys. Rev. Lett.* **98**, 046402 (2007).
97. Scalapino, D. J., White, S. R. & Zhang, S. Insulator, metal, or superconductor: the criteria. *Phys. Rev. B* **47**, 7995–8007 (1993).
98. Huhtinen, K.-E., Herzog-Arbeitman, J., Chew, A., Bernevig, B. A. & Törmä, P. Revisiting flat band superconductivity: dependence on minimal quantum metric and band touchings. *Phys. Rev. B* **106**, 014518 (2022).
99. Simon, S. H. & Rudner, M. S. Contrasting lattice geometry dependent versus independent quantities: ramifications for Berry curvature, energy gaps, and dynamics. *Phys. Rev. B* **102**, 165148 (2020).
100. Tam, M. & Peotta, S. Geometry-independent superfluid weight in multiorbital lattices from the generalized random phase approximation. *Phys. Rev. Res* **6**, 013256 (2024).
101. Mondaini, R., Batrouni, G. G. & Grémaud, B. Pairing and superconductivity in the flat band: Creutz lattice. *Phys. Rev. B* **98**, 155142 (2018).
102. Hofmann, J. S., Berg, E. & Chowdhury, D. Superconductivity, pseudogap, and phase separation in topological flat bands. *Phys. Rev. B* **102**, 201112 (2020).
103. Peri, V., Song, Z.-D., Bernevig, B. A. & Huber, S. D. Fragile topology and flat-band superconductivity in the strong-coupling regime. *Phys. Rev. Lett.* **126**, 027002 (2021).
104. Herzog-Arbeitman, J., Chew, A., Huhtinen, K.-E., Törmä, P. & Bernevig, B. A. Many-body superconductivity in topological flat bands. *arXiv preprint arXiv:2209.00007* (2022).
105. Peotta, S., Huhtinen, K.-E. & Törmä, P. Quantum geometry in superfluidity and superconductivity https://arxiv.org/abs/2308.08248 (2023).
106. Bouzerar, G. & Thumin, M. Hidden symmetry of Bogoliubov de Gennes quasi-particle eigenstates and universal relations in flat band superconducting bipartite lattices https://arxiv.org/abs/2310.06589 (2024).
107. Penttilä, R. P. S., Huhtinen, K.-E. & Törmä, P. Flat-band ratio and quantum metric in the superconductivity of modified Lieb lattices.

Commun. Phys. **8**, https://doi.org/10.1038/s42005-025-01964-y (2024).
108. Jiang, G., Törmä, P. & Barlas, Y. Superfluid weight cross-over and critical temperature enhancement in singular flat bands. *Proc. Natl. Acad. Sci.* **122**, e2416726122 (2025).
109. Cooper, L. N. Bound electron pairs in a degenerate Fermi gas. *Phys. Rev.* **104**, 1189–1190 (1956).
110. Törmä, P., Liang, L. & Peotta, S. Quantum metric and effective mass of a two-body bound state in a flat band. *Phys. Rev. B* **98**, 220511 (2018).
111. Verma, N., Hazra, T. & Randeria, M. Optical spectral weight, phase stiffness, and T_c bounds for trivial and topological flat band superconductors. *Proc. Natl. Acad. Sci. USA* **118**, e2106744118 (2021).
112. Mao, D. & Chowdhury, D. Diamagnetic response and phase stiffness for interacting isolated narrow bands. *Proc. Natl. Acad. Sci. USA* **120**, e2217816120 (2023).
113. Iskin, M. Extracting quantum-geometric effects from Ginzburg-Landau theory in a multiband Hubbard model. *Phys. Rev. B* **107**, 224505 (2023).
114. Chen, S. A. & Law, K. T. Ginzburg-Landau theory of flat-band superconductors with quantum metric. *Phys. Rev. Lett.* **132**, 026002 (2024).
115. Hu, J.-X., Chen, S. A. & Law, K. T. Anomalous coherence length in superconductors with quantum metric. *Commun. Phys.* **8**, .20 (2025).
116. Iskin, M. Coherence length and quantum geometry in a dilute flat-band superconductor *Phys. Rev*. *B* **110**, 144505 (2024).
117. Iskin, M. Pair size and quantum geometry in a multiband Hubbard model. arXiv: 2409.14921 (2024).
118. Thumin, M. & Bouzerar, G. Correlation functions and characteristic length scales in flat band superconductors (2024).
119. Virtanen, P. et al. Superconducting junctions with flat bands. arXiv: 2410.23121 (2024).
120. Xu, Y. et al. Three-dimensional real space invariants, obstructed atomic insulators and a new principle for active catalytic sites. *arXiv preprint arXiv:2111.02433* (2021).
121. Lau, A., Peotta, S., Pikulin, D. I., Rossi, E. & Hyart, T. Universal suppression of superfluid weight by non-magnetic disorder in *s*-wave superconductors independent of quantum geometry and band dispersion. *SciPost Phys.* **13**, 086 (2022).
122. Marsal, Q. & Black-Schaffer, A. M. Enhanced quantum metric due to vacancies in graphene. *Phys. Rev. Lett.* **133**, 026002 (2024).
123. Romeral, J. M., Cummings, A. W. & Roche, S. Scaling of the integrated quantum metric in disordered topological phases. *Phys. Rev. B* **111**, 134201 (2024).
124. Pyykkönen, V. A. J., Peotta, S. & Törmä, P. Suppression of nonequilibrium quasiparticle transport in flat-band superconductors. *Phys. Rev. Lett.* **130**, 216003 (2023).
125. Hofmann, J. S., Berg, E. & Chowdhury, D. Superconductivity, charge density wave, and supersolidity in flat bands with a tunable quantum metric. *Phys. Rev. Lett.* **130**, 226001 (2023).
126. Jiang, G. & Barlas, Y. Pair density waves from local band geometry. *Phys. Rev. Lett.* **131**, 016002 (2023).
127. Chen, W. & Huang, W. Pair density wave facilitated by Bloch quantum geometry in nearly flat band multiorbital superconductors. *Sci. China Phys. Mech. Astron* **66**, 287212 (2023).
128. Shavit, G. & Alicea, J. Quantum geometric Kohn-Luttinger superconductivity. *Phys. Rev. Lett* **134**, 176001 (2025).
129. Jahin, A. & Lin, S.-Z. Enhanced Kohn-Luttinger topological superconductivity in bands with nontrivial geometry. arXiv: 2411.09664 (2024).
130. Roddick, E. & Stroud, D. Effect of phase fluctuations on the low-temperature penetration depth of high- T c superconductors. *Phys. Rev. Lett.* **74**, 1430–1433 (1995).
131. Emery, V. J. & Kivelson, S. A. Superconductivity in bad metals. *Phys. Rev. Lett.* **74**, 3253–3256 (1995).
132. Xiao, Y. & Hao, N. Quantum geometric effects on the Higgs mode in flat-band superconductors. arXiv: 2409.10891 (2024).
133. Wu, F. & Das Sarma, S. Quantum geometry and stability of moiré flatband ferromagnetism. *Phys. Rev. B* **102**, 165118 (2020).
134. Bernevig, B. A. et al. Twisted bilayer graphene. V. Exact analytic many-body excitations in Coulomb Hamiltonians: charge gap, Goldstone modes, and absence of Cooper pairing. *Phys. Rev. B* **103**, 205415 (2021).
135. Khalaf, E., Chatterjee, S., Bultinck, N., Zaletel, M. P. & Vishwanath, A. Charged skyrmions and topological origin of superconductivity in magic-angle graphene. *Sci. Adv.* **7**, eabf5299 (2021).
136. Kitamura, T., Daido, A. & Yanase, Y. Spin-triplet superconductivity from quantum-geometry-induced ferromagnetic fluctuation. *Phys. Rev. Lett.* **132**, 036001 (2024).
137. Kang, J., Oh, T., Lee, J. & Yang, B.-J. Quantum geometric bound for saturated ferromagnetism. arXiv: 2402.07171 (2024).
138. Herzog-Arbeitman, J., Chew, A., Huhtinen, K.-E., Törmä, P. & Bernevig, B. A. Many-body superconductivity in topological flat bands. *arXiv* 2209.00007 (2022).
139. Kang, J. & Vafek, O. Symmetry, maximally localized Wannier states, and a low-energy model for twisted bilayer graphene narrow bands. *Phys. Rev. X* **8**, 031088 (2018).
140. Song, Z.-D., Lian, B., Regnault, N. & Bernevig, B. A. Twisted bilayer graphene. II. Stable symmetry anomaly. *Phys. Rev. B* **103**, 205412 (2021).
141. Huber, S. D. & Altman, E. Bose condensation in flat bands. *Phys. Rev. B* **82**, 184502 (2010).
142. You, Y.-Z., Chen, Z., Sun, X.-Q. & Zhai, H. Superfluidity of bosons in kagome lattices with frustration. *Phys. Rev. Lett.* **109**, 265302 (2012).
143. Julku, A., Bruun, G. M. & Törmä, P. Quantum geometry and flat band Bose-Einstein condensation. *Phys. Rev. Lett.* **127**, 170404 (2021).
144. Julku, A., Salerno, G. & Törmä, P. Superfluidity of flat band Bose-Einstein condensates revisited. *Low. Temp. Phys.* **49**, 701–713 (2023).
145. Julku, A., Bruun, G. M. & Törmä, P. Excitations of a Bose-Einstein condensate and the quantum geometry of a flat band. *Phys. Rev. B* **104**, 144507 (2021).
146. Iskin, M. Quantum-geometric contribution to the Bogoliubov modes in a two-band Bose-Einstein condensate. *Phys. Rev. A* **107**, 023313 (2023).
147. Lukin, I., Sotnikov, A. & Kruchkov, A. Unconventional superfluidity and quantum geometry of topological bosons https://arxiv.org/abs/2307.08748 (2023).
148. Keldysh, L. V. & Kopaev, Y. V. Possible instability of semimetallic state toward Coulomb interaction. *Sov. Phys. Solid State* **6**, 2219 (1965).
149. Halperin, B. I. & Rice, T. M. The Excitonic State at the Semiconductor-Semimetal Transition*. In *Solid State Physics* Vol. 21, (eds Seitz, F., Turnbull, D. & Ehrenreich, H.) 115–192 (Academic Press, 1968).
150. Lozovik, Y. E. & Yudson, V. I. Feasibility of superfluidity of paired spatially separated electrons and holes—new superconductivity mechanism. *Jetp Lett.* **22**, 274 (1975).
151. Eisenstein, J. P. & MacDonald, A. H. Bose-Einstein condensation of excitons in bilayer electron systems. *Nature* **432**, 691 (2004).
152. Neilson, D., Perali, A. & Hamilton, A. R. Excitonic superfluidity and screening in electron-hole bilayer systems. *Phys. Rev. B* **89**, 060502 (2014).
153. Lu, C.-P. et al. Local, global, and nonlinear screening in twisted double-layer graphene. *Proc. Natl. Acad. Sci. USA* **113**, 6623–6628 (2016).
154. Hu, X., Hyart, T., Pikulin, D. I. & Rossi, E. Quantum-metric-enabled exciton condensate in double twisted bilayer graphene. *Phys. Rev. B* **105**, L140506 (2022).
155. Verma, N., Guerci, D. & Queiroz, R. Geometric stiffness in interlayer exciton condensates. *Phys. Rev. Lett.* **132**, 236001 (2024).

156. Bardeen, J., Cooper, L. N. & Schrieffer, J. R. Theory of superconductivity. *Phys. Rev.* **108**, 1175–1204 (1957).
157. Migdal, A. Interaction between electrons and lattice vibrations in a normal metal. *Sov. Phys. JETP* **7**, 996–1001 (1958).
158. Eliashberg, G. Interactions between electrons and lattice vibrations in a superconductor. *Sov. Phys. JETP* **11**, 696–702 (1960).
159. Bradlyn, B. et al. Topological quantum chemistry. *Nature* **547**, 298 (2017).
160. Po, H. C., Vishwanath, A. & Watanabe, H. Symmetry-based indicators of band topology in the 230 space groups. *Nat. Commun.* **8**, 50 (2017).
161. Kruthoff, J., de Boer, J., van Wezel, J., Kane, C. L. & Slager, R.-J. Topological classification of crystalline insulators through band structure combinatorics. *Phys. Rev. X* **7**, 041069 (2017).
162. Vergniory, M. G. et al. A complete catalogue of high-quality topological materials. *Nature* **566**, 480–485 (2019).
163. Zhang, T. et al. Catalogue of topological electronic materials. *Nature* **566**, 475–479 (2019).
164. Tang, F., Po, H. C., Vishwanath, A. & Wan, X. Comprehensive search for topological materials using symmetry indicators. *Nature* **566**, 486–489 (2019).
165. Xu, Y. et al. High-throughput calculations of antiferromagnetic topological materials from magnetic topological quantum chemistry. *Nature* **586**, 702–707 (2020).
166. Narang, P., Garcia, C. A. C. & Felser, C. The topology of electronic band structures. *Nat. Mater.* **20**, 293–300 (2021).
167. Yu, J. et al. Non-trivial quantum geometry and the strength of electron–phonon coupling. *Nat. Phys.* **20**, 1262–1268 (2024).
168. Zhu, P. & Alexandradinata, A. Anomalous shift and optical vorticity in the steady photovoltaic current. *Phys. Rev. B* **110**, 115108 (2024).
169. Neupert, T., Santos, L., Chamon, C. & Mudry, C. Fractional quantum hall states at zero magnetic field. *Phys. Rev. Lett.* **106**, 236804 (2011).
170. Sheng, D. N., Gu, Z.-C., Sun, K. & Sheng, L. Fractional quantum Hall effect in the absence of Landau levels. *Nat. Commun.* **2**, 389 (2011).
171. Regnault, N. & Bernevig, B. A. Fractional Chern insulator. *Phys. Rev. X* **1**, 021014 (2011).
172. Sun, K., Gu, Z., Katsura, H. & Das Sarma, S. Nearly flatbands with nontrivial topology. *Phys. Rev. Lett.* **106**, 236803 (2011).
173. Tang, E., Mei, J.-W. & Wen, X.-G. High-temperature fractional quantum hall states. *Phys. Rev. Lett.* **106**, 236802 (2011).
174. Ozawa, T. & Mera, B. Relations between topology and the quantum metric for Chern insulators. *Phys. Rev. B* **104**, 045103 (2021).
175. Haldane, F. D. M. Fractional quantization of the Hall effect: a hierarchy of incompressible quantum fluid states. *Phys. Rev. Lett.* **51**, 605 (1983).
176. Wang, J., Cano, J., Millis, A. J., Liu, Z. & Yang, B. Exact landau level description of geometry and interaction in a flatband. *Phys. Rev. Lett.* **127**, 246403 (2021).
177. Ledwith, P. J., Vishwanath, A. & Parker, D. E. Vortexability: a unifying criterion for ideal fractional Chern insulators. *Phys. Rev. B* **108**, 205144 (2023).
178. Estienne, B., Regnault, N. & Crépel, V. Ideal Chern bands as Landau levels in curved space. *Phys. Rev. Res* **5**, L032048 (2023).
179. Liu, Z., Mera, B., Fujimoto, M., Ozawa, T. & Wang, J. Theory of generalized landau levels and implication for non-abelian states. arXiv: 2405.14479 (2024).
180. Claassen, M., Lee, C. H., Thomale, R., Qi, X.-L. & Devereaux, T. P. Position-momentum duality and fractional quantum Hall effect in chern insulators. *Phys. Rev. Lett.* **114**, 236802 (2015).
181. Northe, C., Palumbo, G., Sturm, J., Tutschku, C. & Hankiewicz, E. M. Interplay of band geometry and topology in ideal Chern insulators in the presence of external electromagnetic fields. *Phys. Rev. B* **105**, 155410 (2022).
182. Ji, G. & Yang, B. Quantum metric induced hole dispersion and emergent particle-hole symmetry in topological flat bands. *arXiv preprint arXiv:2409.08324* (2024).
183. Andrews, B., Raja, M., Mishra, N., Zaletel, M. P. & Roy, R. Stability of fractional Chern insulators with a non-Landau level continuum limit. *Phys. Rev. B* **109**, 245111 (2024).
184. Simon, S. H., Harper, F. & Read, N. Fractional Chern insulators in bands with zero Berry curvature. *Phys. Rev. B* **92**, 195104 (2015).
185. Cai, J. et al. Signatures of fractional quantum anomalous Hall states in twisted MoTe2. *Nature* **622**, 63–68 (2023).
186. Zeng, Y. et al. Thermodynamic evidence of fractional Chern insulator in moiré MoTe2. *Nature* **622**, 69–73 (2023).
187. Park, H. et al. Observation of fractionally quantized anomalous Hall effect. *Nature* **622**, 74–79 (2023).
188. Xu, F. et al. Observation of integer and fractional quantum anomalous Hall states in twisted bilayer MoTe2. *Phys. Rev. X* **13**, 031037 (2023).
189. Ji, Z. et al. Local probe of bulk and edge states in a fractional Chern insulator. *Nature* **635**, 578–583 (2024).
190. Kang, K. et al. Evidence of the fractional quantum spin hall effect in moiré mote2. *Nature* **628**, 522–526 (2024).
191. Park, H. et al. Ferromagnetism and topology of the higher flat band in a fractional Chern insulator. *Nat. Phys.* **21**, 549–555 (2024).
192. Xiao, D., Liu, G.-B., Feng, W., Xu, X. & Yao, W. Coupled spin and valley physics in monolayers of MoS_2 and other group-VI dichalcogenides. *Phys. Rev. Lett.* **108**, 196802 (2012).
193. Wu, F., Lovorn, T., Tutuc, E., Martin, I. & MacDonald, A. Topological insulators in twisted transition metal dichalcogenide homobilayers. *Phys. Rev. Lett.* **122**, 086402 (2019).
194. Pan, H., Wu, F. & Das Sarma, S. Band topology, Hubbard model, Heisenberg model, and Dzyaloshinskii-Moriya interaction in twisted bilayer WSe_2. *Phys. Rev. Res* **2**, 033087 (2020).
195. Li, H., Kumar, U., Sun, K. & Lin, S.-Z. Spontaneous fractional Chern insulators in transition metal dichalcogenide moiré superlattices. *Phys. Rev. Res* **3**, L032070 (2021).
196. Zhang, Y., Liu, T. & Fu, L. Electronic structures, charge transfer, and charge order in twisted transition metal dichalcogenide bilayers. *Phys. Rev. B* **103**, 155142 (2021).
197. Devakul, T., Crépel, V., Zhang, Y. & Fu, L. Magic in twisted transition metal dichalcogenide bilayers. *Nat. Commun.* **12**, 6730 (2021).
198. Wang, T., Devakul, T., Zaletel, M. P. & Fu, L. Topological magnets and magnons in twisted bilayer $MoTe_2$ and WSe_2. arXiv: 2306.02501 (2023).
199. Reddy, A. P., Alsallom, F., Zhang, Y., Devakul, T. & Fu, L. Fractional quantum anomalous Hall states in twisted bilayer $MoTe_2$ and WSe_2. *Phys. Rev. B* **108**, 085117 (2023).
200. Dong, J., Wang, J., Ledwith, P. J., Vishwanath, A. & Parker, D. E. Composite Fermi liquid at zero magnetic field in twisted $MoTe_2$. *Phys. Rev. Lett.* **131**, 136502 (2023).
201. Qiu, W.-X., Li, B., Luo, X.-J. & Wu, F. Interaction-driven topological phase diagram of twisted Bilayer $MoTe_2$. *Phys. Rev. X* **13**, 041026 (2023).
202. Wang, T. et al. Topology, magnetism and charge order in twisted $MoTe_2$ at higher integer hole fillings (2023).
203. Reddy, A. P. & Fu, L. Toward a global phase diagram of the fractional quantum anomalous Hall effect. *Phys. Rev. B* **108**, 245159 (2023).
204. Wang, C. et al. Fractional Chern insulator in twisted Bilayer $MoTe_2$. *Phys. Rev. Lett.* **132**, 036501 (2024).
205. Yu, J. et al. Fractional Chern insulators versus nonmagnetic states in twisted bilayer $MoTe_2$. *Phys. Rev. B* **109**, 045147 (2024).
206. Xu, C., Li, J., Xu, Y., Bi, Z. & Zhang, Y. Maximally localized Wannier functions, interaction models, and fractional quantum anomalous Hall effect in twisted bilayer $MoTe_2$. *Proc. Natl. Acad. Sci. USA* **121**, e2316749121 (2024).

207. Abouelkomsan, A., Reddy, A. P., Fu, L. & Bergholtz, E. J. Band mixing in the quantum anomalous Hall regime of twisted semiconductor bilayers. *Phys. Rev. B* **109**, L121107 (2024).
208. Jia, Y. et al. Moiré fractional Chern insulators. I. First-principles calculations and continuum models of twisted bilayer $MoTe_2$. *Phys. Rev. B* **109**, 205121 (2024).
209. Zhang, X.-W. et al. Polarization-driven band topology evolution in twisted $MoTe_2$ and WSe_2. *Nat. Commun.* **15**, 4223 (2024).
210. Wu, A.-K., Sarkar, S., Wan, X., Sun, K. & Lin, S.-Z. Quantum-metric-induced quantum Hall conductance inversion and reentrant transition in fractional Chern insulators. *Phys. Rev. Res* **6**, L032063 (2024).
211. Li, H. et al. Contrasting twisted bilayer graphene and transition metal dichalcogenides for fractional Chern insulators: an emergent gauge picture. *Phys. Rev. B* **109**, 245131 (2024).
212. Lu, Z. et al. Fractional quantum anomalous Hall effect in multilayer graphene. *Nature* **626**, 759–764 (2024).
213. Xie, J. et al. Tunable fractional Chern insulators in rhombohedral graphene superlattices. *Nat. Mater.* **24**, 1042–1048 (2025).
214. Choi, Y. et al. Superconductivity and quantized anomalous Hall effect in rhombohedral graphene. *Nat.* **639**, 342–347 (2025).
215. Lu, Z. et al. Extended quantum anomalous Hall states in graphene/hBN moiré superlattices *Nature* **637**, 1090–1095 (2024).
216. Park, Y., Kim, Y., Chittari, B. L. & Jung, J. Topological flat bands in rhombohedral tetralayer and multilayer graphene on hexagonal boron nitride moiré superlattices. *Phys. Rev. B* **108**, 155406 (2023).
217. Herzog-Arbeitman, J. et al. Moiré fractional Chern insulators. ii. first-principles calculations and continuum models of rhombohedral graphene superlattices. *Phys. Rev. B* **109**, 205122 (2024).
218. Kwan, Y. H., Yu, J., Herzog-Arbeitman, J., Efetov, D. K., Regnault, N. & Bernevig, B. A. Moir´e, arXiv https://doi.org/10.48550/arXiv.2312.11617 (2023).
219. Yu, J., Herzog-Arbeitman, J., Kwan, Y. H., Regnault, N. & Bernevig, B. A. Moir´e, arXiv https://doi.org/10.48550/arXiv.2407.13770 (2024).
220. Guo, Z., Lu, X., Xie, B. & Liu, J. Fractional Chern insulator states in multilayer graphene moiré superlattices. *Phys. Rev. B* **110**, 075109 (2024).
221. Zhou, B., Yang, H. & Zhang, Y.-H. Fractional quantum anomalous Hall effects in rhombohedral multilayer graphene in the moiré. *arXiv* https://doi.org/10.48550/arXiv.2311.04217 (2024).
222. Dong, J. et al. Anomalous Hall crystals in rhombohedral multilayer graphene i: Interaction-driven Chern bands and fractional quantum hall states at zero magnetic field. *Phys. Rev. Lett* **133**, 206503 (2024).
223. Soejima, T. et al. Anomalous Hall crystals in rhombohedral multilayer graphene ii: General mechanism and a minimal model. *Phys. Rev. B* **110**, 205124 (2024).
224. Huang, K., Sarma, S. D. & Li, X. Impurity-induced thermal crossover in fractional Chern insulators. *arXiv* https://doi.org/10.48550/arXiv.2409.04349 (2024).
225. Tan, T., May-Mann, J. & Devakul, T. Wavefunction approach to the fractional anomalous Hall crystal. *arXiv* https://doi.org/10.48550/arXiv.2409.06775 (2024).
226. Dong, Z., Patri, A. S. & Senthil, T. Theory of Quantum Anomalous Hall Phases in Pentalayer Rhombohedral Graphene Moir\'e Structures. *Phys. Rev. Lett* **133**, 206502 (2024).
227. Huang, K., Li, X., Sarma, S. D. & Zhang, F. Self-consistent theory of fractional quantum anomalous hall states in rhombohedral graphene. *Phys. Rev. B* **110**, 115146 (2024).
228. Sarma, S. D. & Xie, M. Thermal crossover from a Chern insulator to a fractional Chern insulator in pentalayer graphene. *Phys. Rev. B* **110**, 155148 (2024).
229. Xie, M. & Sarma, S. D. Integer and fractional quantum anomalous Hall effects in pentalayer graphene. *Phys. Rev. B* **109**, L241115 (2024).
230. Dong, Z., Patri, A. S. & Senthil, T. Stability of anomalous Hall crystals in multilayer rhombohedral graphene. *Phys. Rev. B* **110**, 205130 (2024).
231. Kudo, K., Nakai, R. & Nomura, K. Quantum anomalous, spin, and valley Hall effects in pentalayer rhombohedral graphene moir\'e superlattices. *Phys. Rev. B* **110**, 245135 (2024).
232. Zhou, B. & Zhang, Y.-H. New classes of quantum anomalous Hall crystals in multilayer graphene. *arXiv* https://doi.org/10.48550/arXiv.2411.04174 (2024).
233. Resta, R. Polarization fluctuations in insulators and metals: new and old theories merge. *Phys. Rev. Lett.* **96**, 137601 (2006).
234. King-Smith, R. D. & Vanderbilt, D. Theory of polarization of crystalline solids. *Phys. Rev. B* **47**, 1651–1654 (1993).
235. Aebischer, C., Baeriswyl, D. & Noack, R. M. Dielectric catastrophe at the Mott transition. *Phys. Rev. Lett.* **86**, 468–471 (2001).
236. Komissarov, I., Holder, T. & Queiroz, R. The quantum geometric origin of capacitance in insulators. *Nat. Commun.* **15**, 4621 (2024).
237. Verma, N. & Queiroz, R. Instantaneous response and quantum geometry of insulators. *arXiv:2403.07052* (2024).
238. Hetényi, B. & Lévay, P. Fluctuations, uncertainty relations, and the geometry of quantum state manifolds. *Phys. Rev. A* **108**, 032218 (2023).
239. Resta, R. Geometry and Topology in Electronic Structure Theory. *Lecture Notes* (2022).
240. Verma, N. & Queiroz, R. Framework to Measure Quantum Metric from Step Response. *Phys. Rev. Lett* **134**, 106403 (2025).
241. Verma, N. & Queiroz, R. Instantaneous response and quantum geometry of insulators. *arXiv* https://doi.org/10.48550/arxiv.2403.07052 (2025).
242. Tam, P. M., Herzog-Arbeitman, J. & Yu, J. Corner charge fluctuation as an observable for quantum geometry and entanglement in two-dimensional insulators. *Phys. Rev. Lett* **133**, 246603 (2024).
243. Onishi, Y. & Fu, L. Topological bound on structure factor. *Phys. Rev. Lett* **133**, 206602 (2024).
244. Onishi, Y. & Fu, L. Fundamental bound on topological gap. *Phys. Rev. X* **14**, 011052 (2024).
245. Souza, I. & Vanderbilt, D. Dichroic f-sum rule and the orbital magnetization of crystals. *Phys. Rev. B* **77**, 054438 (2008).
246. Thonhauser, T., Ceresoli, D., Vanderbilt, D. & Resta, R. Orbital magnetization in periodic insulators. *Phys. Rev. Lett.* **95**, 137205 (2005).
247. Xiao, D., Shi, J. & Niu, Q. Berry phase correction to electron density of states in solids. *Phys. Rev. Lett.* **95**, 137204 (2005).
248. Onishi, Y. & Fu, L. Quantum weight: A fundamental property of quantum many-body systems. *Phys. Rev. Res* **7**, 023158 (2025).
249. Asteria, L. et al. Measuring quantized circular dichroism in ultracold topological matter. *Nat. Phys.* **15**, 449–454 (2019).
250. Noziéres, P. & Pines, D. Electron interaction in solids. general formulation. *Phys. Rev.* **109**, 741–761 (1958).
251. Noziéres, P. & Pines, D. A dielectric formulation of the many body problem: application to the free electron gas. *Nuovo Cim* **9**, 470–490 (1958).
252. Hazra, T., Verma, N. & Randeria, M. Bounds on the superconducting transition temperature: applications to twisted bilayer graphene andcold atoms. *Phys. Rev. X* **9**, 031049 (2019).
253. Alexander, K. & Shinsei, R. Spectral sum rules reflect topological and quantum-geometric invariants. *arXiv* https://arxiv.org/abs/2312.17318 (2023).
254. Sachs, R. G. & Austern, N. Consequences of guage invariance for radiative transitions. *Phys. Rev.* **81**, 705–709 (1951).
255. Iskin, M. Geometric mass acquisition via a quantum metric: an effective-band-mass theorem for the helicity bands. *Phys. Rev. A* **99**, 053603 (2019).
256. Kivelson, S. Wannier functions in one-dimensional disordered systems: application to fractionally charged solitons. *Phys. Rev. B* **26**, 4269–4277 (1982).

257. Martin, R. M. Electronic Structure. https://doi.org/10.1017/CBO9780511805769 (2004).
258. Onishi, Y. & Fu, L. Universal relation between energy gap and dielectric constant. *Phys. Rev. B.* **110**, 155107 (2024).
259. Souza, I., Martin, R. M. & Stengel, M. Optical bounds on many-electron localization. *SciPost Phys.* **18**, 127 (2025).
260. Kohn, W. Cyclotron resonance and de Haas-van alphen oscillations of an interacting electron gas. *Phys. Rev.* **123**, 1242–1244 (1961).
261. Mendez-Valderrama, J. F., Mao, D. & Chowdhury, D. Low-energy optical sum rule in moiré graphene. *Phys. Rev. Lett.* **133**, 196501 (2024).
262. Mao, D., Mendez-Valderrama, J. F. & Chowdhury, D. Is the low-energy optical absorption in correlated insulators controlled by quantum geometry? arXiv: 2410.16352 (2024).
263. Holder, T., Kaplan, D. & Yan, B. Consequences of time-reversal-symmetry breaking in the light-matter interaction: Berry curvature, quantum metric, and diabatic motion. *Phys. Rev. Res* **2**, 033100 (2020).
264. Zhang, Y. et al. Photogalvanic effect in Weyl semimetals from first principles. *Phys. Rev. B* **97**, 241118 (2018).
265. Kaplan, D., Holder, T. & Yan, B. Twisted photovoltaics at terahertz frequencies from momentum shift current. *Phys. Rev. Res* **4**, 013209 (2022).
266. Kaplan, D., Holder, T. & Yan, B. Nonvanishing subgap photocurrent as a probe of lifetime effects. *Phys. Rev. Lett.* **125**, 227401 (2020).
267. Kaplan, D., Holder, T. & Yan, B. Unifying semiclassics and quantum perturbation theory at nonlinear order. *SciPost Phys.* **14**, 082 (2023).
268. Onsager, L. Interpretation of the de Haas-van Alphen effect. *Lond. Edinb. Dublin Philos. Mag. J. Sci.* **43**, 1006–1008 (1952).
269. Roth, L. M. Semiclassical theory of magnetic energy levels and magnetic susceptibility of Bloch electrons. *Phys. Rev.* **145**, 434 (1966).
270. Mikitik, G. & Sharlai, Y. V. Manifestation of Berry's phase in metal physics. *Phys. Rev. Lett.* **82**, 2147 (1999).
271. Gao, Y. & Niu, Q. Zero-field magnetic response functions in Landau levels. *Proc. Natl. Acad. Sci. USA* **114**, 7295–7300 (2017).
272. Fuchs, J.-N., Piéchon, F. & Montambaux, G. Landau levels, response functions and magnetic oscillations from a generalized Onsager relation. *SciPost Phys.* **4**, 024 (2018).
273. Xiao, D., Chang, M.-C. & Niu, Q. Berry phase effects on electronic properties. *Rev. Mod. Phys.* **82**, 1959 (2010).
274. Hwang, Y., Rhim, J.-W. & Yang, B.-J. Geometric characterization of anomalous Landau levels of isolated flat bands. *Nat. Commun.* **12**, 6433 (2021).
275. Rhim, J.-W., Kim, K. & Yang, B.-J. Quantum distance and anomalous Landau levels of flat bands. *Nature* **584**, 59–63 (2020).
276. Jung, J., Lim, H. & Yang, B.-J. Quantum geometry and Landau levels of quadratic band crossings. *Phys. Rev. B* **109**, 035134 (2024).
277. Oh, C.-g., Rhim, J.-W. & Yang, B.-J. Revisiting the magnetic responses of bilayer graphene from the perspective of the quantum distance. *Phys. Rev. B* **110**, 155412 (2024).
278. Chang, M.-C. & Niu, Q. Berry phase, hyperorbits, and the Hofstadter spectrum: semiclassical dynamics in magnetic Bloch bands. *Phys. Rev. B* **53**, 7010 (1996).
279. Rhim, J.-W. & Yang, B.-J. Classification of flat bands according to the band-crossing singularity of Bloch wave functions. *Phys. Rev. B* **99**, 045107 (2019).
280. Rhim, J.-W. & Yang, B.-J. Singular flat bands. *Adv. Phys: X* **6**, 1901606 (2021).
281. Hwang, Y., Rhim, J.-W. & Yang, B.-J. General construction of flat bands with and without band crossings based on wave function singularity. *Phys. Rev. B* **104**, 085144 (2021).
282. Hwang, Y., Jung, J., Rhim, J.-W. & Yang, B.-J. Wave-function geometry of band crossing points in two dimensions. *Phys. Rev. B* **103**, L241102 (2021).
283. McCann, E. & Koshino, M. The electronic properties of bilayer graphene. *Rep. Prog. Phys.* **76**, 056503 (2013).
284. Novoselov, K. S. et al. Unconventional quantum Hall effect and Berry's phase of 2π in bilayer graphene. *Nat. Phys.* **2**, 177–180 (2006).
285. Korshunov, A. et al. Softening of a flat phonon mode in the kagome ScV6Sn6. *Nat. Commun.* **14**, 6646 (2023).
286. Chan, S. M., Grémaud, B. & Batrouni, G. G. Designer flat bands: Topology and enhancement of superconductivity. *Phys. Rev. B* **106**, 104514 (2022).
287. Li, Z. C. F., Deng, Y., Chen, S. A., Efetov, D. K. & Law, K. T. Flat band josephson junctions with quantum metric. arXiv: 2404.09211 (2024).
288. Solnyshkov, D. D. et al. Quantum metric and wave packets at exceptional points in non-hermitian systems. *Phys. Rev. B* **103**, 125302 (2021).
289. Liao, Q. et al. Experimental measurement of the divergent quantum metric of an exceptional point. *Phys. Rev. Lett.* **127**, 107402 (2021).
290. Amelio, I. & Goldman, N. Lasing in non-hermitian flat bands: Quantum geometry, coherence, and the fate of Kardar-Parisi-Zhang physics. *Phys. Rev. Lett.* **132**, 186902 (2024).
291. Tesfaye, I. & Eckardt, A. Quantum geometry of bosonic Bogoliubov quasiparticles. arXiv: 2406.12981 (2024).
292. Yu, M. et al. Experimental measurement of the quantum geometric tensor using coupled qubits in diamond. *Nat. Sci. Rev.* **7**, 254–260 (2019).
293. Gianfrate, A. et al. Measurement of the Quantum Geometric Tensor and of the Anomalous Hall Drift. *Nature* **578**, 381–385 (2020).
294. Zheng, W. et al. Measuring quantum geometric tensor of non-Abelian system in superconducting circuits. *Chin. Phys. Lett.* **39**, 100202 (2022).
295. Yi, C.-R. et al. Extracting the quantum geometric tensor of an optical raman lattice by bloch-state tomography. *Phys. Rev. Res* **5**, L032016 (2023).
296. Cuerda, J., Taskinen, J. M., Källman, N., Grabitz, L. & Törmä, P. Observation of quantum metric and non-hermitian berry curvature in a plasmonic lattice. *Phys. Rev. Res* **6**, L022020 (2024).
297. Tanaka, M. et al. Kinetic Inductance, Quantum Geometry, and Superconductivity in Magic-Angle Twisted Bilayer Graphene. *arXiv e-prints* arXiv:2406.13740 (2024).
298. Fang, Y., Cano, J. & Ghorashi, S. A. A. Quantum geometry induced nonlinear transport in altermagnets. *Phys. Rev. Lett.* **133**, 106701 (2024).
299. Bałut, D., Bradlyn, B. & Abbamonte, P. Quantum entanglement and quantum geometry measured with inelastic x-ray scattering. *Phys. Rev. B* **111**, 125161 (2025).
300. Kang, M. et al. Measurements of the quantum geometric tensor in solids. *Nat. Phys.* **21**, 110–117 (2025).
301. Kim, S. et al. Direct measurement of the quantum metric tensor in solids. *Science* **388**, 1050–1054 (2025).
302. Tovmasyan, M., Peotta, S., Liang, L., Törmä, P. & Huber, S. D. Preformed pairs in flat Bloch bands. *Phys. Rev. B* **98**, 134513 (2018).
303. Han, Z., Herzog-Arbeitman, J., Bernevig, B. A. & Kivelson, S. A. Quantum Geometric Nesting'' and Solvable Model Flat-Band Systems. *Phys. Rev. X* **14**, 041004 (2024).
304. Salerno, G., Ozawa, T. & Törmä, P. Drude weight and the many-body quantum metric in one-dimensional Bose systems. *Phys. Rev. B* **108**, L140503 (2023).
305. Faugno, W. N. & Ozawa, T. Geometric characterization of many body localization. arXiv: 2311.12280 (2023).
306. Tam, P. M., Herzog-Arbeitman, J. & Yu, J. Quantum geometry and entanglement in two-dimensional insulators: a view from the corner charge fluctuation. *arXiv preprint arXiv:2406.17023* (2024).
307. Wu, X.-C., Cai, K.-L., Cheng, M. & Kumar, P. Corner charge fluctuations and many-body quantum geometry. arXiv: 2408.16057 (2024).

308. Niedermeier, M., Nairn, M., Flindt, C. & Lado, J. L. Quantum computing topological invariants of two-dimensional quantum matter. *Phys. Rev. Res* **6**, 043288 (2024).
309. Chen, T., Ding, H.-T., Shen, R., Zhu, S.-L. & Gong, J. Direct probe of topology and geometry of quantum states on ibm q. arXiv: 2403.14249 (2024).
310. Lim, L.-K., Fuchs, J.-N. & Montambaux, G. Geometry of Bloch states probed by stückelberg interferometry. *Phys. Rev. A* **92**, 063627 (2015).
311. Piéchon, F., Raoux, A., Fuchs, J.-N. & Montambaux, G. Geometric orbital susceptibility: quantum metric without Berry curvature. *Phys. Rev. B* **94**, 134423 (2016).
312. Jankowski, W. J. & Slager, R.-J. Quantized integrated shift effect in multigap topological phases. *Phys. Rev. Lett.* **133**, 186601 (2024).
313. Yogendra, K. B., Baskaran, G. & Das, T. Fractional Wannier orbitals and tight-binding gauge fields for Kitaev honeycomb superlattices with flat Majorana bands. *Phys. Rev. X* **15**, 031020 (2025).
314. Gong, Z.-H., Du, Z. Z., Sun, H.-P., Lu, H.-Z. & Xie, X. C. Nonlinear transport theory at the order of quantum metric. arXiv: 2410.04995 (2024).
315. Bouhon, A., Timmel, A. & Slager, R.-J. Quantum geometry beyond projective single bands. arXiv: 2303.02180 (2023).

Acknowledgements

B.A.B. was supported by the Gordon and Betty Moore Foundation through Grant No. GBMF8685 towards the Princeton theory program, the Gordon and Betty Moore Foundation's EPiQS Initiative (Grant No. GBMF11070), the Office of Naval Research (ONR Grant No. N00014-20-1-2303), the Global Collaborative Network Grant at Princeton University, the Simons Investigator Grant No. 404513, the BSF Israel US foundation No. 2018226, the NSF-MERSEC (Grant No. MERSEC DMR 2011750), by a grant from the Simons Foundation (SFI-MPS-NFS-00006741-01, B.A.B.) in the Simons Collaboration on New Frontiers in Superconductivity, and the Schmidt Foundation at the Princeton University. P.T. was supported by the Research Council of Finland under project number 339313 and by Jane and Aatos Erkko Foundation, Keele Foundation, and Magnus Ehrnrooth Foundation as part of the SuperC collaboration, as well as by a grant from the Simons Foundation (SFI-MPS-NFS-00006741-12, P.T.) in the Simons Collaboration on New Frontiers in Superconductivity. B.-J.Y. was supported by Samsung Science and Technology Foundation under Project No. SSTF-BA2002-06, National Research Foundation of Korea (NRF) grants funded by the government of Korea (MSIT) (Grants No. NRF-2021R1A5A1032996), and GRDC(Global Research Development Center) Cooperative Hub Program through the National Research Foundation of Korea(NRF) funded by the Ministry of Science and ICT(MSIT) (RS-2023 00258359). E.R. was supported by the US Department of Energy, Office of Basic Energy Sciences, via Award DE-SC0022245, and thanksthe Kavli Institute for Theoretical Physics (KITP), supported in part by NSF grant PHY-2309135, and the Aspen Center for Physics, supported by NSF Grant PHY-2210452, where part of this work was performed. R.Q. was supported by the National Science Foundation under Award No. DMR-2340394, and the NSF-MRSEC (DMR-2011738), and the U.S. Department of Energy (DOE), Office of Science, Basic Energy Sciences (BES), under award DE-SC0019443. J.Y.'s work at Princeton University is supported by the Gordon and Betty Moore Foundation through Grant No. GBMF8685 towards the Princeton theory program. J.Y.'s work at University of Florida is supported by startup funds at University of Florida.

Author contributions

J.Y., B.A.B., R.Q., E.R., P.T., and B.-J.Y. all contribute to the writing of this review.

Competing interests

The authors declare no competing interests.

Additional information

Supplementary information The online version contains supplementary material available at https://doi.org/10.1038/s41535-025-00801-3.

Correspondence and requests for materials should be addressed to Jiabin Yu.

Reprints and permissions information is available at http://www.nature.com/reprints